



Analysis of the dust–methane two-phase coupling blowdown effect at different air duct positions in an excavation anchor synchronous tunnel

Wen Nie^{1,2} · Qianqian Xue^{1,2} · Lidian Guo^{1,2} · Faxin Li³ · Yun Hua^{1,2} · Qiang Liu^{1,2} · Ning Sun^{1,2} · Chenwang Jiang^{1,2} · Fengning Yu^{1,2}

Received: 7 May 2022 / Accepted: 23 May 2023 / Published online: 27 June 2023
© The Author(s), under exclusive licence to Springer-Verlag GmbH Germany, part of Springer Nature 2023

Abstract

Bolter miners are being increasingly used. Unfortunately, this mining technology causes a considerable amount of air pollution (especially by methane and dust) during excavation. In this study, the multiphase coupling field of airflow–dust–methane for different distances between the pressure air outlet and the working face (L_p) was simulated by using the FLUENT software. The migration law of pollutants in the multiphase coupling field was analyzed, and the distance parameters between the pressure air outlet and the working face were optimized. Finally, the simulation results were verified based on the field measurement results. We found that the blowdown effect was more obvious when $14\text{ m} \leq L_p < 16\text{ m}$ compared with other conditions. The peak value of dust concentration within this distance range was the smallest (44.4% lower than the highest peak value, which was verified when $L_p = 18\text{ m}$), while the methane concentration was $< 0.6\%$. A high-concentration area (where methane concentration $> 0.75\%$), identified near the walking part of the bolter miner, was 13 m shorter than the largest (when $L_p = 18\text{ m}$). Therefore, we determined that the optimal blowdown distance would be $14\text{ m} \leq L_p < 16\text{ m}$. Within this range, the dust removal and methane dilution effects are optimal, effectively improving the tunnel air quality and providing a safe and clean environment for mine workers.

Keywords Excavation and anchor synchronous tunnel · Multi-phase coupling · Temporal-spatial evolution law · Optimal blowdown distance · Air pollution control

Introduction

A harmonious coexistence has always been necessary for a sustainable development of human society (Niu et al. 2021; Nie et al. 2022; Peng et al. 2022); at the same time, a healthy and safe working environment is at the basis of long-term economic stability (Cui et al. 2019; Xue et al. 2021). Mineral resources have a fundamental role in supporting the current energy demand (which has increased significantly), especially in terms of coal resources (Nie et al. 2022; Hua et al. 2022; Liu et al. 2019). In China, to improve tunneling efficiency and meet the requirements of high-yield coal resources, mining methods and technologies have been gradually developing towards informatization, automation, and mechanization (Xu et al. 2020; Zheng et al. 2016, 2021).

The popularization and application of bolter miners in mining areas under suitable conditions has improved the level of underground equipment's automation and tunneling efficiency (Fig. 1), and has promoted a sustainable development of coal

Responsible Editor: Shimin Liu

✉ Lidian Guo
sdustguold@163.com

¹ College of Safety and Environmental Engineering, Shandong University of Science and Technology, Qingdao 266590, Shandong Province, China

² State Key Laboratory of Mining Disaster Prevention and Control Co-Founded By Shandong Province and the Ministry of Science and Technology, Shandong University of Science and Technology, Qingdao 266590, China

³ College of Energy and Mining Engineering, Shandong University of Science and Technology, Qingdao 266590, Shandong Province, China

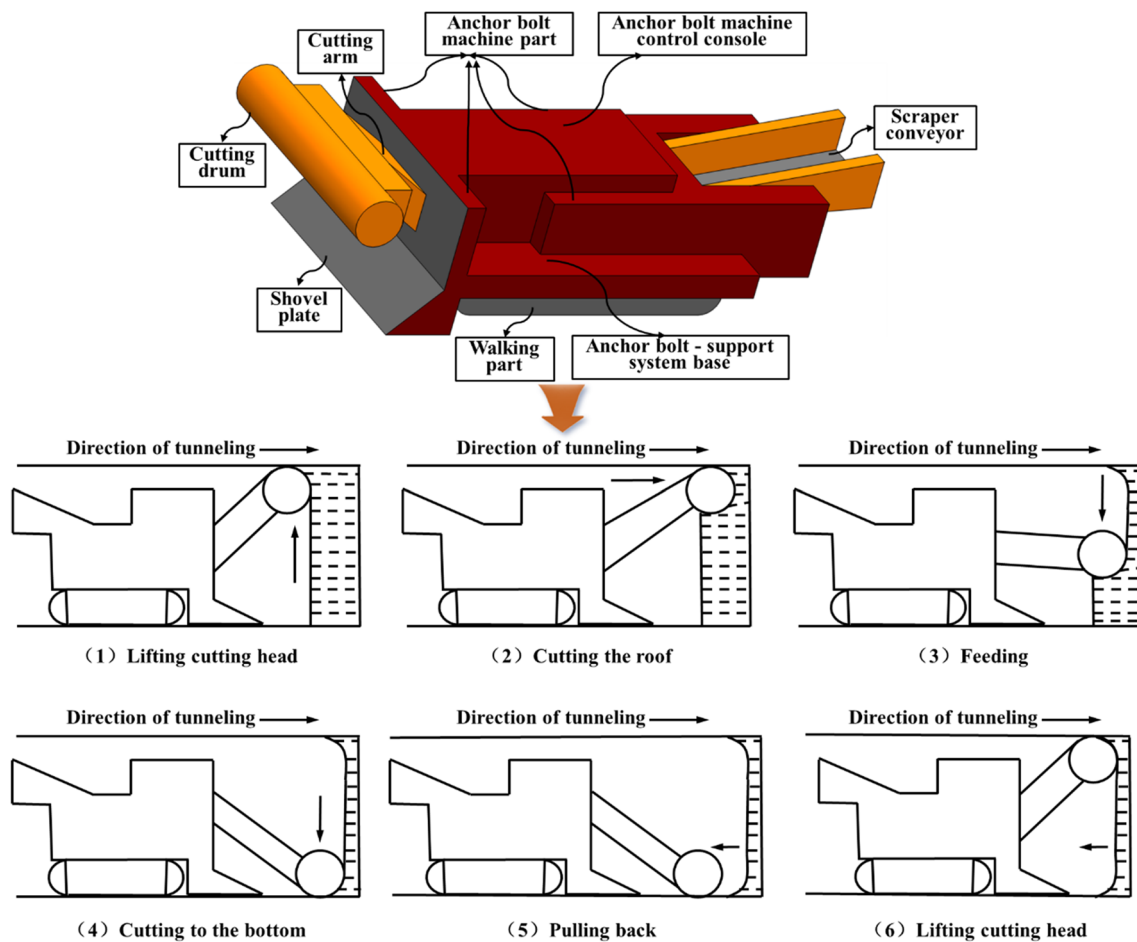


Fig. 1 Diagram of one-time tunneling process by cyclic cutting of bolter-miner

mines (Finkelman et al. 2021; Li et al. 2015). However, during bolter miners' operations, the contact area between the roller's cutting teeth and the coal wall is relatively large (Xu et al. 2019, 2023; Nie et al. 2023a, b). This configuration can result in high dust concentrations in the working face (Paluchamy et al. 2021; Seaman et al. 2020; Trecheraa et al. 2020). In addition, large amounts of dust are typically lifted by the roller's rotating force (Li et al. 2013). Notably, the methane emission rate tends to increase during mining, easily causing methane overrun and negatively affecting the working environment (production safety in particular) (Nie et al. 2023c; Liu et al. 2023; Niu et al. 2023). At this stage, dust–methane pollution in the excavation face can be reduced by a ventilation system (Nie et al. 2023d). Single-forced ventilation systems are commonly used in current methane-containing excavation tunnels (Chang et al. 2020; Fan and Liu 2021; Huang et al. 2021). This system includes a local fan (located in the intake airflow roadway) that introduces fresh air into the tunnel through a pressure air duct. After impacting the working face, this air mixes with methane and dust and is discharged outside of the tunnel (Han et al. 2019; Wang et al. 2019a, b). Ultimately,

this process helps meeting the breathing requirements of mine workers. In the absence of local fans, methane would accumulate in the tunnel near the air duct due to its buoyancy: single forced ventilation systems effectively prevent explosions caused by electric sparks in areas of high methane concentration. Due to their high safety, simple layout, convenient installation, and other characteristics, single-forced ventilation systems are increasingly being installed in methane-containing tunnels, making research on this topic a top priority (Liu and Liu 2020; Ma et al. 2022). Importantly, the distance between the pressure air outlet and the working face determines the distribution of the airflow field and the effects of pollutant emissions (Li et al. 2020; Omid et al. 2020; Tu et al. 2021). The optimization of this parameter is therefore fundamental to reduce dust and methane pollution and ensure an improvement of air quality in the tunnel environment. Overall, reducing dust and methane pollution is a top priority in coal mine safety management (Nie et al. 2023e; Xu et al. 2023; Ren et al. 2022).

Some previous studies have focused on the optimization of bolter miners and on the reduction of tunnel pollution, providing a reliable basis for further investigations

(Liu et al. 2021a, b). For instance, considering a tunnel environment characterized by high dust concentrations, poor working conditions, and an inefficient, slow elimination of dust through ventilation, Jia et al. proposed a new dust control approach, consisting in the installation of dry dust removal equipment on the panel of excavation and on the anchor. After applying such approach for more than six months, they observed a 90% dust removal rate, which indicated an effective improvement of the environment in correspondence of the working face (Jia 2017). Niu et al. used a long pressure and short pumping dust-control system to control dust pollution at the working face. The dust control parameters of the system were optimized, and the installation layout was improved according to the production process conditions and the dust movement characteristics in correspondence of the continuous mining face. The dust collector of a continuous miner was used to control dust production during coal cutting, achieving a remarkable dust reduction effect (Niu and Yang 2019). Liu et al. analyzed the multi-phase flow state of a dusty airflow and, at the same time, applied spraying dust-settling on a continuous mining face: the spraying of a continuous miner was effectively improved. A BA405 fan and KC306 hollow nozzles were positioned at the two corners of a spade plate and optimized through a field test (Liu and Chen 2019). Zhou et al. used the CFD method to evaluate the effect of the curtain setback distance on airflow and methane distribution in a working face (both in the presence and in the absence of a continuous miner) based on full-scale ventilation gallery data. They compared and analyzed the methane distribution under three different curtain setback distances, determined the methane accumulation area at the working face, and verified the principle of the CFD model (Zhou et al. 2015). Lu et al. simulated methane and dust diffusion along a roadway based on the CFD model of a continuous mining face: the diffusion and accumulation of methane and dust under the influence of a continuous miner's auxiliary ventilation were evaluated and discussed. The best dilution of methane and dust under such conditions was obtained by combining a scrubber fan in suction mode with a brattice (Lu et al. 2017). Wang et al. used the CFD method to simulate and study the airflow pattern and the diffusion characteristics of respirable dust in an underground heading face driven with a continuous miner, and identified the main reasons behind high concentrations of dust. Based on this, they proposed a new ventilation arrangement and a dust mitigation strategy to achieve the best mitigation effect (Wang et al. 2019a, b).

A lot of research has been conducted worldwide on methane emission, distribution, and accumulation in tunnels during excavation, with the aim of solving the problem of high methane concentrations (Liu et al.

2021a, b). Ji et al. analyzed the influencing factors of methane emissions: by using a numerical simulation software (COSMOL Multiphysics), they investigated the methane flow law in a roadway under different tunneling speeds. Their results, showing that the excavation speed can influence the distribution of methane pressure, provided a theoretical basis for the prevention of methane accidents during roadway excavation (Ji and Ye 2018). Zhou et al. constructed three CFD models of face ventilation blowing curtain setback distances and validated them based on experimental data collected in a full-scale ventilation test facility, obtaining detailed airflow and methane distribution information (Zhou et al. 2015). To calculate the pressure and molecule velocity of methane during methane drainage operations, Adel et al. studied the methane flow in a coal block, successfully simulating the movements of fluid and methane molecules in a porous medium (Adel et al. 2016). Hasheminasab et al. established a numerical simulation model by using the software ANSYS, investigating the detailed laws regulating the airflow field and methane concentration distribution in a working coal face section of an underground mine in the presence of an auxiliary ventilation system. Then, according to the geometric shapes of different brattice curtains and of the exhaust ducted fan, they determined the ventilation parameters, the airflow field distribution under each ventilation scheme, the primary ventilation parameters, and the methane release rate, verifying the effectiveness of the ventilation system in diluting pollutants in dead corners and highly polluted areas (Hasheminasab et al. 2019). Mishra et al. used the CFD simulation software to study the impact of five important geomining parameters (i.e., air velocity, methane emission rate, width, surface roughness, and mine gallery inclination) on methane layering and dispersion in hard coal underground mines. Their aim was to determine the key parameters linked to safe levels of methane diffusion, so to improve the design of underground coal mines and prevent methane explosions (Mishra et al. 2018). Kurnia et al. established a mathematical model of relevant methane diffusion in an excavation tunnel with discrete methane emission sources by using CFD. On this basis, they were able to determine the methane emission rates and the constant methane emission rates for several emission sources in different locations and for different emission amounts. Based on the laws of airflow and methane diffusion in the mining face obtained by the CFD method, relevant mitigation and recovery strategies were proposed: the installation of a suction duct equipped with a brattice curtain. The methane concentrations in the mining face and at the outlet of the suction duct were also evaluated, so as to

determine the best suction duct height, setback distance, and suction velocity for controlling them (Kurnia et al. 2014, 2016). Du et al. used the FLUENT software to conduct a numerical simulation of the airflow field and of methane distribution in a single heading roadway: they obtained the laws regulating the airflow field, the methane concentration distribution, and the formation of high-concentration methane areas, and compared the methane concentrations in the roadway with those on the return air side. Through an orthogonal test, moreover, they determined the influence of the air duct diameter, of the air duct outlet velocity, of the distance between the air duct outlet and the working face, and of the air duct hanging position on methane concentration, so as to envision the best possible ventilation layout (Du 2017).

Specific studies on the dust diffusion law and dust control have also been conducted. Fan et al. investigated the dispersion characteristics of dust pollutants in a typical coal roadway during the functioning of an auxiliary ventilation system. Each dust particle was traced, and particle collisions were reconstructed via a hard-sphere model and a direct simulation based on the Monte Carlo method. The bulk movements of dust particles were simulated; then, the simulation results were validated by comparing them with field measurement results (Fan et al. 2020). Torno et al. studied the airflow and dust diffusion around two different types of conveyor belts by applying the CFD method; also, they analyzed the impact of dust diffusion pollution on the loss of treated product and on the maintenance of equipment and facilities (Torno et al. 2020). Candra et al. used the CFD method to evaluate the airflow flow and the dust diffusion behavior in an excavation working face both in the presence and in the absence of an auxiliary ventilation system; furthermore, they studied the dust concentration distribution in the excavation working face under six different ventilation schemes and determined an effective method to direct dust particles away from the mining face (Candra et al. 2014). Lu et al. used the CFD method to simulate and study the impact of the cutting position of a roadheader on dust diffusion during its operation, evaluated the distribution characteristics of dust in a tunnel at nine representative cutting positions, and identified highly dust-polluted areas in the proximity of different cutting positions. Their aim was to provide a basis for implementing dynamic dust prevention measures and achieving a sustainable, clean production (Lu et al. 2022). Gui et al. used the CFD method to simulate the dust distribution characteristics at a typical roadheader mining face in the presence of an auxiliary ventilation system with an air curtain. They optimized the relevant parameters of the air curtain generator, finding that the improvement of the air curtain had a significant impact on the air flow field, dust distribution, and the amount of particulate matter (PM_{2.5})

in the front part of the roadway (within ~15 m of the heading face) (Gui et al. 2020). Hu et al. used the CFD method to simulate the airflow field and dust distribution around a road-header driver in an actual excavation tunnel, finding that the driver was located at the intersection of three airflow vortices. Furthermore, they defined the change rule of dust concentration around the road-header driver (Hu et al. 2019). Li et al. performed a numerical simulation to analyze the laws of airflow motion and dust distribution under three ventilation modes (i.e., forced ventilation, exhaust ventilation, and combined forced fan (with a long duct)–short duct exhaust ventilation), optimized the local ventilation layout of the excavation face, and determined the best position for the air duct opening of the combined forced fan (with a long duct)–short duct exhaust ventilation system (Li et al. 2014).

Despite the interesting findings of previous research, there are still some important themes to explore. First of all, studies on excavation anchor synchronous tunnels have mainly focused on the design and application of bolter miners. The diffusion of dust and methane pollutants in such tunnels should be investigated further: the presents scarcity of detailed information does not allow an efficient improvement of the tunnel environment. Secondly, the movement and accumulation of dust and methane, as well as specific prevention methods, have been investigated; however, research on the coupled diffusion of dust and methane in tunnels has not been carried out. Finally, single-forced ventilation is usually applied in tunnels characterized by high methane concentrations to remove pollution. However, after considering the interaction between various pollutants, we can infer the further investigation on the optimal position of the pressure air duct inlet is necessary.

In this study, we considered the 81,309 tunnel of Baode Coal Mining Co., Ltd. and used a numerical simulation method (i.e., CFD) to explore the airflow field structure and the diffusion characteristics of pollutants released by a bolter-miner. The pollutant conditions at different distances from the pressure air outlet to the working face were compared, and the optimal position of the pressure air duct required for the elimination of pollution was determined. Finally, the result accuracy was verified by comparing the simulation and field measurement data.

Numerical simulation model of an excavation and anchor synchronous tunnel

According to the relevant mathematical model of the dust–methane two-phase flow field and the physical model of the tunnel, we used the FLUENT 16.0 software to simulate the airflow field structure and the dust–methane distribution of an excavation and anchor synchronous tunnel (i.e., a

tunnel excavated with a bolter miner). Different distances between the pressure air outlet and the working face (L_p) were considered to this scope.

Selection of the mathematical model

Selection of the mathematical model for the gas phase

In correspondence of the excavation face, air and methane were both characterized by a turbulent flow: a complex eddy and three-dimensional unsteady flow, generally irregular (Diego et al. 2011; Launder and Spalding 1974). Therefore, the $\kappa - \epsilon$ equations were used to reflect the fluid transient fluctuating value in the Reynolds time-averaged equations (Lafuente et al. 2020; Wang 2010; Xu et al. 2016).

The variables in the momentum and continuity equations had to be decomposed into the sum of the fluctuation and mean values, which can be expressed as $u_i = U_i + u_i'$, $p = P + p'$. The Reynolds averaged N-S equation was obtained by substituting the mean values U_i , P , and the fluctuation values u_i' , p' into the momentum and continuity equations (Shu et al. 2023; Wang et al. 2022; Huang et al. 2022).

Continuity equation for the gas phase:

$$\frac{\partial U}{\partial x} + \frac{\partial V}{\partial y} + \frac{\partial W}{\partial z} = 0 \tag{1}$$

Momentum equation for the gas phase:

$$\frac{\partial U_i}{\partial t} + U_j \frac{\partial U_i}{\partial x_j} = -\frac{1}{\rho} \frac{\partial P}{\partial x_i} + \nu \frac{\partial^2 U_i}{\partial x_j \partial x_j} + \frac{1}{\rho} \frac{\partial(-\overline{\rho u_i' u_j'})}{\partial x_j} - \overline{\rho u_i' u_j'} \tag{2}$$

Turbulent kinetic energy equation (κ equation):

$$\frac{\partial(\rho\kappa)}{\partial t} + \frac{\partial(\rho\kappa u_i)}{\partial x_i} = \frac{\partial}{\partial x_j} \left[\left(\mu + \frac{\mu_i}{\sigma_\kappa} \right) \frac{\partial \kappa}{\partial x_j} \right] + G_\kappa - \rho\epsilon \tag{3}$$

Turbulent energy dissipation rate equation (ϵ equation):

$$\frac{\partial(\rho\epsilon)}{\partial t} + \frac{\partial(\rho\epsilon u_i)}{\partial x_i} = \frac{\partial}{\partial x_j} \left[\left(\mu + \frac{\mu_i}{\sigma_\epsilon} \right) \frac{\partial \epsilon}{\partial x_j} \right] + \rho C_1 E \epsilon - \rho C_2 \frac{\epsilon^2}{\kappa + \sqrt{\nu \epsilon}} \tag{4}$$

In the above equation, $C_1 = \max \left[0.43, \frac{\eta}{\eta + 5} \right]$, $\eta = E \frac{\kappa}{\epsilon}$, C_2 is a constant, $E = \sqrt{2 E_{ij} E_{ij}}$, G_κ is the turbulent kinetic energy production term derived by the velocity gradient of mean motion (i.e., $G_\kappa = \mu_i E^2$), and σ_κ and σ_ϵ are the turbulent Prandtl numbers of the κ and ϵ equations, respectively (Wang et al. 2022; Liu et al. 2022). For the calculations, we considered the following empirical values: $C_2 = 1.9$, $\sigma_\kappa = 1.0$, and $\sigma_\epsilon = 1.2$.

The value of μ_i in the above equation was determined according to the following equation:

$$\mu_i = \rho C_\mu \frac{\kappa^2}{\epsilon} \tag{5}$$

where C_μ is no longer a constant, but rather a functional expression related to the average change rate and the turbulent flow field (κ and ϵ): $C_\mu = \frac{1}{A_0 + A_S U^* \kappa / \epsilon}$, where $A_0 = 4.0$, $A_S = \sqrt{6} \cos \phi$, $\phi = \frac{1}{3} \arccos \left(\sqrt{6} w \right)$, $w = \frac{E_{ij} E_{jk} E_{ki}}{\sqrt{E_{ij} E_{ij}}}$, $E_{ij} = \frac{1}{2} \left(\frac{\partial u_i}{\partial x_j} + \frac{\partial u_j}{\partial x_i} \right)$, $U^* = \sqrt{E_{ij} E_{ij} + \overline{\Omega_{ij} \Omega_{ij}}}$, $\overline{\Omega_{ij}} = \overline{\Omega_{ij}} - \epsilon_{ijk} \omega_k$, and $\overline{\Omega_{ij}} = \overline{\Omega_{ij}} - 2 \epsilon_{ijk} \omega_k$. In these last equations, $\overline{\Omega_{ij}}$ is the time-averaged rate-of-turn tensor obtained from a reference frame with an angular velocity ω_k . Another feature of the proposed model is that, in the case of a flow field without rotation, the second term of the equation radical for U^* is 0, which introduces the influence of rotation (Lu et al. 2017; Liu and Chen 2019).

Component transport equation:

$$\frac{\partial(\rho c_s u)}{\partial x} + \frac{\partial(\rho c_s v)}{\partial y} + \frac{\partial(\rho c_s w)}{\partial z} = \frac{\partial}{\partial x} \left(D_s \frac{\partial \rho c_s}{\partial x} \right) + \frac{\partial}{\partial y} \left(D_s \frac{\partial \rho c_s}{\partial y} \right) + \frac{\partial}{\partial z} \left(D_s \frac{\partial \rho c_s}{\partial z} \right) + S_s \tag{6}$$

where c_s is the volume concentration of component s , S_s is the component productivity, ρc_s is the mass concentration of the component, and D_s is the diffusion coefficient of the component.

Selection of the mathematical model for the particulate phase

When using the FLUENT software for the simulation, the gas was regarded as a continuous phase, while the dust particles were regarded as a discrete phase. For the calculation of the discrete phase, the particle trajectory was solved by integrating the differential equation of the strength state of the dust particle in Lagrange coordinates (Abbasi and Abbasi 2007; Chang et al. 2019; Wei 2018).

The equilibrium equation of the force of dust particles in the airflow field is as follows:

$$m_p \frac{du_p}{dt} = \sum F = F_d + F_g + F_f + F_s + F_m + F_x \tag{7}$$

where m is the mass of the dust particles (in kg), u is the movement rate of the dust particles (in m/s), and $\sum F$, F_d , F_g , F_f , F_s , F_m , and F_x are the resultant force, resistance, gravity, buoyancy, Saffman lift force, Magnus lift force, and other related forces, respectively (in N). Notably, F_x includes the thermophoretic and additional mass forces and other forces, and its order of magnitude is small, which can be ignored in this study. Other forces are represented by the following formulas.

Resistance:

$$F_2 = \frac{1}{2} C_d C_p A_p \rho (u_g - u_p) |u_g - u_p| \tag{8}$$

where C_d is the resistance coefficient, C_p is the dynamic shape factor (for which we considered a value of 1), A_p is the base of the windward side of the dust particles (in m^2), u_g is the airflow velocity (in m/s), and u_p is the velocity of dust particles (in m/s). Importantly, the resistance coefficient C_d is related to the Reynolds number: $C_d = f(Re_p); Re_p = \frac{\rho d_p |u_g - u_p|}{\mu}$ (where Re_p is the Reynolds number or the relative Reynolds number of the dust particles (dimensionless) and d_p is the diameter of dust particles (in m)).

The two basic forces related to the dust particles (i.e., gravity and buoyancy) are expressed in the equation below:

$$F_f = mg - \rho g V_p = mg \frac{\rho_p}{\rho_p} - \rho g \frac{m}{\rho_p} = \frac{mg(\rho_p - \rho)}{\rho_p} = \frac{d_p^3 g (\rho_p - \rho)}{6} \tag{9}$$

where g is the acceleration of gravity (in $m\ s^{-2}$), V_p is the volume of the dust particles (in m^3), and ρ is the density of the gas phase fluid (in kg/m^3).

The Saffman lift force is derived from the difference between the velocity gradient of the gas-phase fluid flow and the air velocity of dust particle migration and diffusion. It can be expressed as follows:

$$F_s = 1.61 \sqrt{\mu \rho} d_p^2 (u - u_p) \sqrt{\left| \frac{du}{dy} \right|} \tag{10}$$

Meanwhile, the Magnus lift force has the same order of magnitude as the gravity produced by the rotation of the dust particles in the gas-phase fluid. It can be expressed as follows:

$$F_m = \frac{\pi d_p^3 \rho \omega (u - u_p)}{2} \tag{11}$$

Establishment of the physical model and mesh division

According to the actual situation of the excavation and anchor synchronous tunnel, we established a physical model with a 1:1 scale through the SolidWorks software (Fig. 2a). To determine the optimal distance between the pressure air duct and the working face, based on the original physical model, we derived five models by changing the position of the pressure air duct (Fig. 2b). Each physical model consisted of five parts: a fully mechanized excavation face, a pressure air duct, an MB670/217 type bolter-miner, a reversed loader, and a DSP1080 belt conveyor. Positive values along the x direction indicated that the left wall of the tunnel pointed toward the side of the pressure air duct, while positive values along the y direction indicated that the tunnel floor pointed toward the tunnel roof; moreover, positive values along the z direction indicated that the working face pointed toward the tunnel exit. The relevant parameters of the physical model are shown in Fig. 2a.

Through the ICEM-CFD software, the above physical model was meshed by finite element mesh division. To achieve the best effect possible, the most complicated areas were divided by local regional meshing (Fig. 3a): the total number of meshes for five groups of physical models was ~ 3.9 million. After the mesh optimization, the maximum mesh quality was ≥ 0.999 , the average mesh quality was ~ 0.735 , and there were no negative

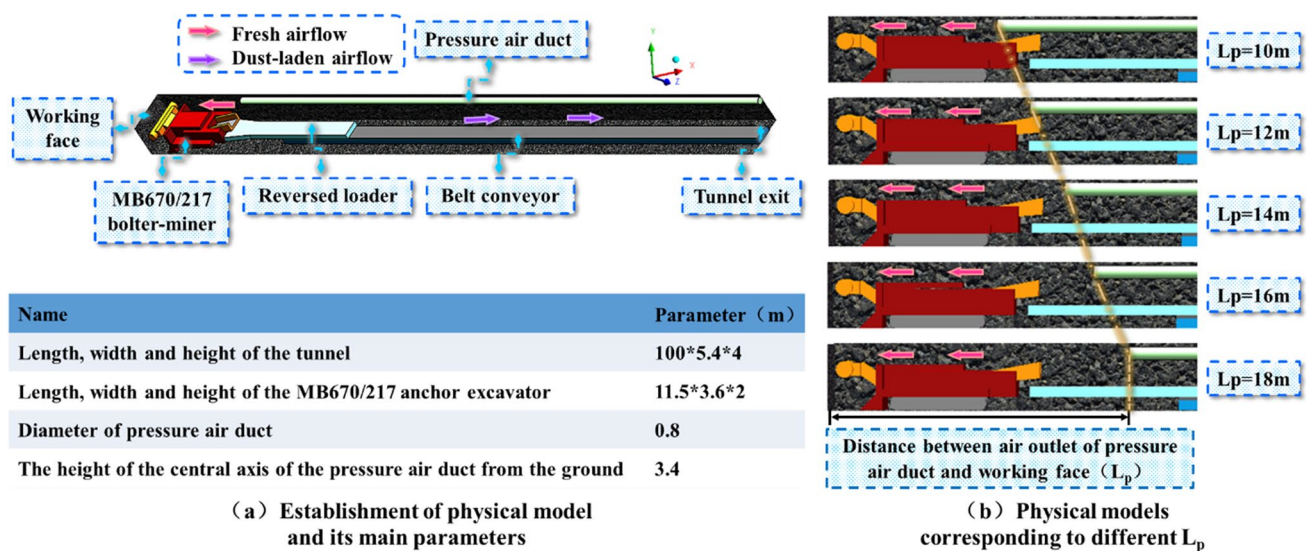
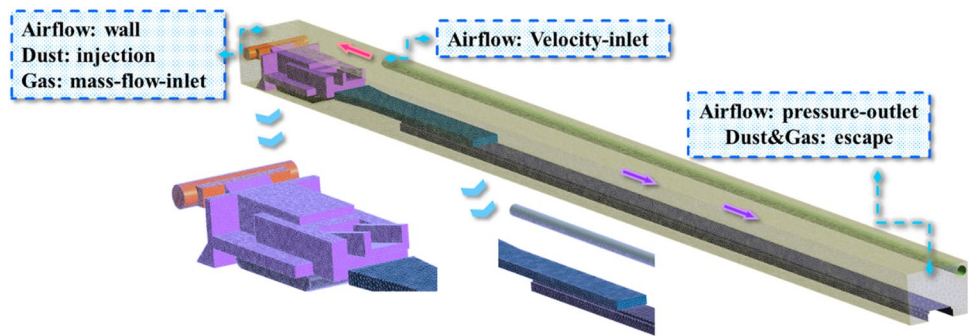
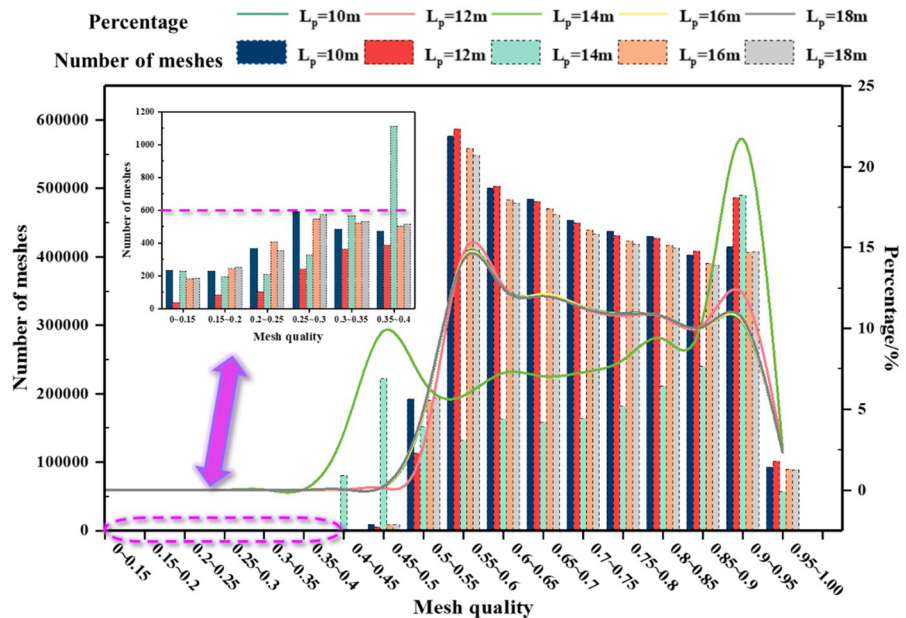


Fig. 2 Construction of physical model

Fig. 3 Diagram of mesh division and quality distribution



(a) Meshing results and boundary conditions



(b) Distribution map of quality index of finite element mesh

meshes. Through the analysis of the mesh quality and quantity distribution (Fig. 3b), the following conclusions could be drawn: most of the mesh quality was concentrated in the range of 0.4–1.0; moreover, ~99.9% of the total meshes had values >0.4, and the mesh quality was good, meeting the simulation conditions of the 81,309 excavation face.

Setting of boundary conditions

For our simulation, performed with the FLUENT software, accurate information about the dust and methane sources, the particle size distribution, the methane emissions, the initial airflow velocity, and other relevant parameters was required. According to the geological report of Baode Coal Mining Co., Ltd. and the production data of the 81,309 excavation face, the methane content of the main minable coal seams was relatively high: the relative methane emissions during excavation were 13.16 m³/t, while the absolute methane emissions were 106.62 m³/min.

The absolute methane emissions correspond to the amount of methane emitted from the mine in a unit of time (m³/day or m³/min). The relative methane emissions correspond instead to the monthly average daily output of coal under normal production conditions (in m³/t). The variation law of the methane content in coal seams in relation to the coal seam elevation is $W = 0.0068 \times H + 2.8347$, and the methane content gradient is 0.68 m³/(t·100 m). It is expected that after pre-extraction, the residual methane content in the area to be excavated would be 4.3 m³/t. Considering national industry standards, as well as the simplicity of sampling and measurement, the speed, and accuracy of operation, we identified the filter membrane sampling method as an ideal solution to be applied during dust production in excavation working faces. According to the characteristics of dust production in the comprehensive excavation face, dust sampling should be carried out 30 min after the start of the operations. To this aim, an AKFC-92A mine dust sampler and an organic filter membrane with a diameter of 40 mm should be used. Notably, the sampling

flow rate should be maintained stable at 20 L/min during the process. The dust in the head-on area of the 81,309 tunnel of Baode Coal Mining Co., Ltd. was sampled. After sealing and storage, the particle size and dispersion of the dust particle samples were tested in the laboratory using a Mastersizer 3000 laser particulate size description analyzer (Fig. 4). The particle size in the head-on area presented a normal distribution, and the particle size ranged between 0.169 and 48.3 μm; furthermore, the mean particle diameter was 7.35 μm. During excavation production, the head-on area was the main source of dust and methane: a large amount of pollution, accounting for > 80% of the total pollution production, was produced there over a long period of time. Therefore, the head-on area

was identified as the main source of methane and dust during the simulation period. The boundary conditions required for simulation (e.g., tunnel head-on and exit, air duct outlet, and tunnel wall) were mainly set according to the actual production conditions of the excavation face. The air duct inlet was set as a velocity-inlet, while the tunnel exit was set as a pressure-outlet (because it was far from the head-on and the airflow velocity is stable). The tunnel wall and the equipment surface had a blocking effect on the airflow and did not interact with dust and methane; therefore, they were considered as solid walls without slip for the simulation. All the relevant boundary condition settings are shown in Fig. 3a, and the main boundary condition parameters are shown in Table 1.

Fig. 4 Histogram of dust particle size distribution

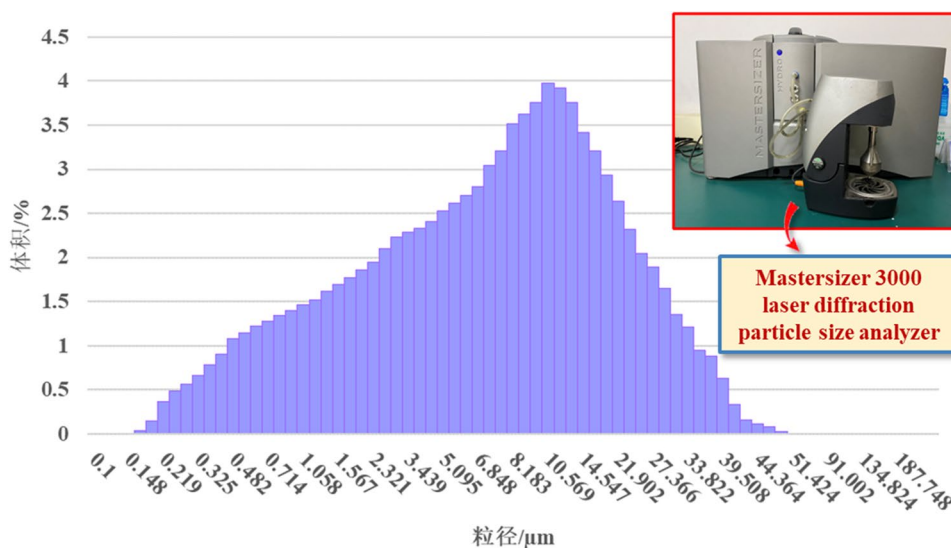


Table 1 Main boundary condition parameters

Project	Name	Parameter
General	Gravity (m/s ²)	9.81
Model	Viscous model	k-epsilon
	Discrete phase model	
	Species model	Species transport
Materials	Air	
	CH ₄	
	Coal-hv	
Boundary conditions	Air duct inlet boundary type	Velocity-inlet
	Dust and gas source boundary type	Mass-flow-inlet
	Tunnel exit boundary type	Pressure-outlet
	Tunnel boundary	DPM: reflect
	Equipment surface	DPM: reflect
Point properties	Total flow rate (kg/s)	0.02
	Min. diameter (m)	1.69 × 10 ⁻⁷
	Max. diameter (m)	4.83 × 10 ⁻⁵
	Mean. diameter (m)	7.35 × 10 ⁻⁶
	Temperature (K)	300

Numerical simulation results: airflow–dust–methane multi-phase coupling in the excavation and anchor synchronous tunnel

To pertinently explore the local characteristics and migration of the airflow–dust–methane multi-phase coupling in the excavation and anchor synchronous tunnel (by combining the requirements of present working face regulations), we considered an air outlet of the pressure air duct positioned 14 m away from the working face.

Local characteristics and velocity distribution of the airflow field

The post processing software CFD-Post was used to elaborate the simulation results. A streamline represented the airflow trace, while an arrow represented the airflow direction. According to the simulation results (Fig. 5), we were able to describe the local characteristics of the airflow.

- (1) Since the pressure air duct was close to the wall of the tunnel, after the airflow was ejected from the

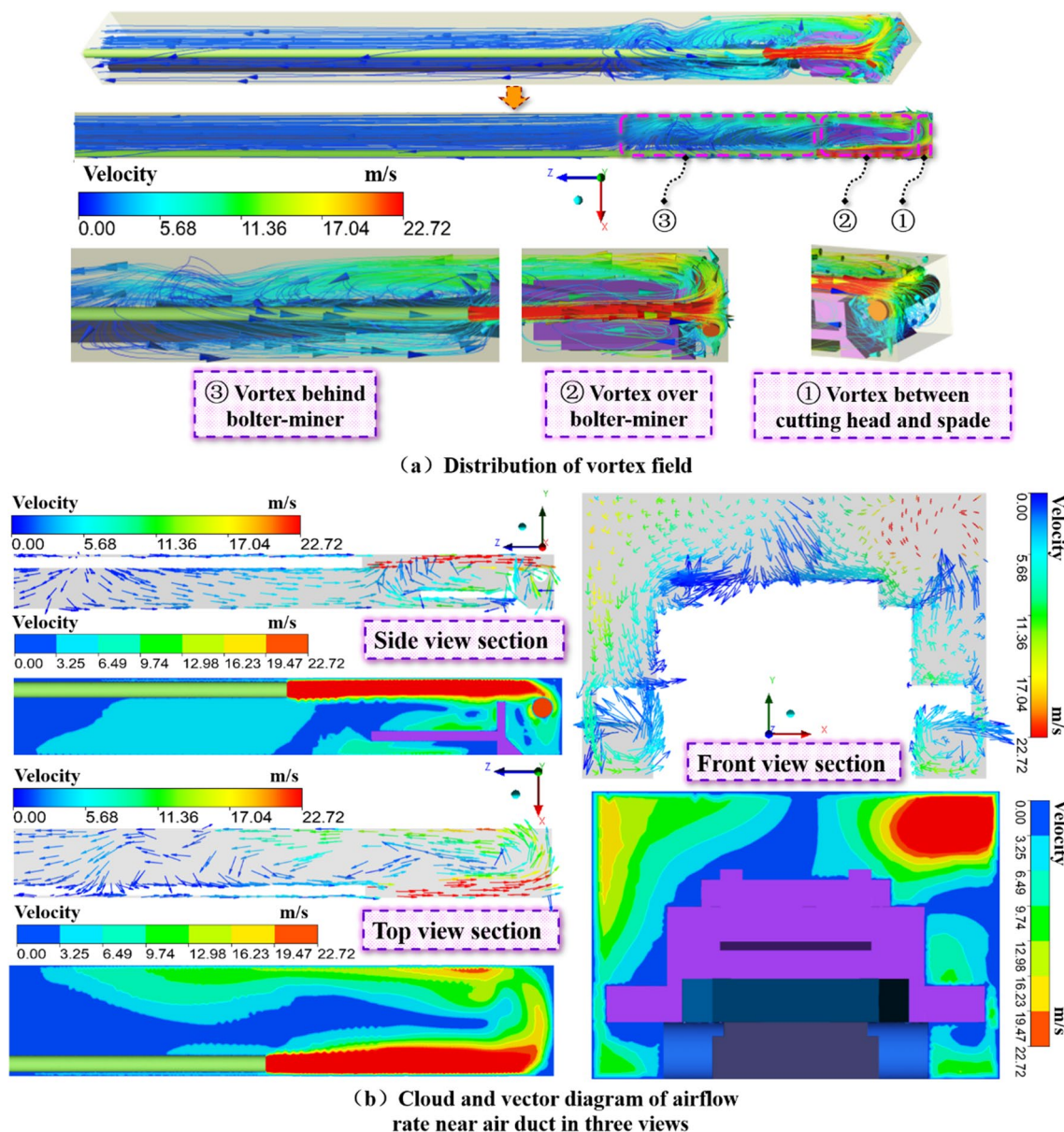


Fig. 5 Cloud chart of local characteristics of airflow and distribution of airflow rate

pressure air outlet at a velocity of 22.72 m/s, a wall-attachment jet formed along the tunnel. When an air jet was sprayed to the working face, the low-velocity airflow near the pressure air duct was continuously sucked into the jet area and moved forward together with the high-velocity jet. As the airflow moved forward, its kinetic energy gradually weakened; however, due to the continuous airflow inhalation in the jet area, the air velocity fluctuated up and down while the air jet moved forward and its attenuation was slow. At the same time, due to the limited space in the tunnel, the airflow bypassed the cutting head of the bolter-miner and flowed along the left wall of the tunnel toward the exit.

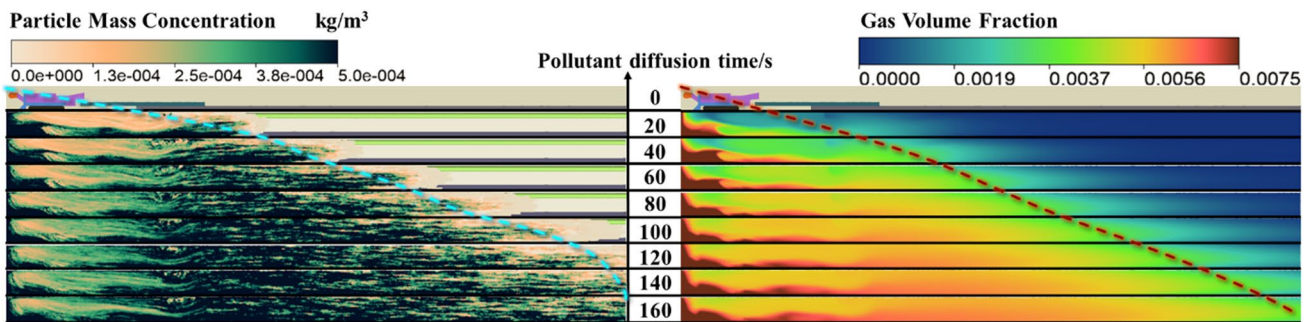
- (2) There were three vortices in the tunnel. The first (a small-scale vortex) occurred within the area at ≤ 3 m away from the working face, more precisely between the cutting head and the spade plate, and was generated by the huge energy change caused by the cutting head during the working process. The second vortex occurred within the area 0–13 m away from the working face: due to the entrainment effect of pressure air outlet, some airflow was entrained into the jet area,

leading to the formation of a vortex field above the bolter-miner. The third vortex occurred within the area 13–38 m away from the working face: the air velocity at the top of the airflow field was higher than that at the bottom; this, combined with the energy interference caused by the reversed loader, caused the formation of a relatively large vortex field in the rear area of the bolter-miner.

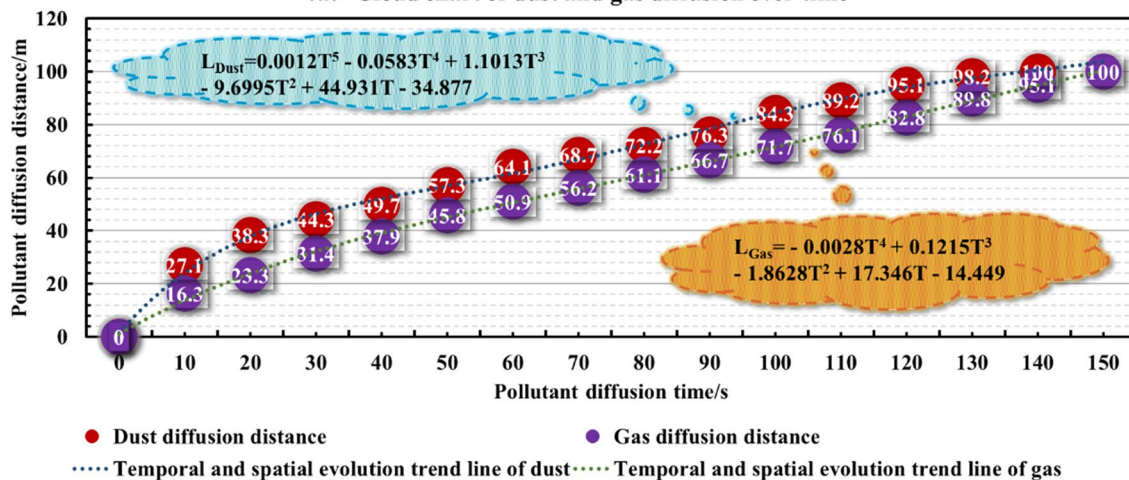
- (3) Within the area 38–100 m away from the working face, since the airflow was not affected by the air jet nor by the vortex field near the working face, the kinetic energy of the airflow decayed gradually, resulting in a decrease of the air velocity. When the air velocity finally dropped to 0.7 m/s, the air continued to flow steadily toward the tunnel exit in the form of a relatively stable airflow field.

Temporal–spatial evolution laws of the dust–methane two-phase diffusion

Dust–methane migration was greatly affected by the airflow field, and the diffusion of methane led to the formation of a vortex area in the airflow field. According to the



(a) Cloud chart of dust and gas diffusion over time



(b) Diagram of temporal-spatial evolution law of dust and gas

Fig. 6 Diagram of temporal-spatial evolution law of dust-gas diffusion

cloud chart derived from the dust–methane simulation results, the curve chart of relevant data (Fig. 6), and the local characteristics of the airflow field, we determined the characteristics of dust–methane migration and the associated temporal–spatial evolution laws. In addition, we obtained the fitting equations of the dust–methane temporal–spatial evolution, in which L and T represent the diffusion distance of pollutants in the tunnel and the diffusion time of pollutants, respectively.

- (1) The high-velocity jet from the pressure air duct quickly dispersed the dust at the working face and blew it to the opposite side of the pressure air duct (i.e., the left side of the tunnel). This resulted in a significantly higher dust concentration on the left side of the tunnel, rather than on the air duct side. After the blown dust hit the left corner of the working face, most of it deposited due to the impact. However, part of the small dust particles moved toward the tunnel exit, transported by the airflow. At $T = 138$ s, a dust concentration of > 200 mg/m³ was distributed throughout the whole tunnel. The fitting equation of the temporal–spatial evolution of dust was expressed by L_{Dust} ($L_{\text{Dust}} = 0.0012T^5 - 0.0583T^4 + 1.1013T^3 - 9.6995T^2 + 44.931T - 34.877$). According to the fitting equation, when $T < 30$ s, the dust diffusion rate increases over time; once $T = 30$ s, however, the dust gradually enters a stable airflow field, and the overall diffusion rate gradually decreases.
- (2) The dust that continued moving toward the tunnel exit passed through the vortex field above the bolter-miner and a small part of it was involved in such vortex field: the dust concentration at the top of the tunnel was higher than that at the bottom. A remaining, large amount of dust was not affected by the vortex field in front of the bolter-miner and continued to move backward transported by the airflow. After passing through the large vortex field behind the bolter-miner, a large amount of dust was deposited there. As the air velocity decayed and tended to balance, the ability of airflow to carry dust was weakened. At this moment, the dust which was not affected by the vortex field accumulated at the bottom, on the left side of the tunnel. At $T = 218$ s, the dust concentration stabilized.
- (3) Due to the inflow of a high-velocity air jet at the pressure air outlet, the lowest methane concentration occurred in the jet area (between the pressure air outlet and the working face), where it was $\leq 0.25\%$. However, under the influence of three vortices, the

lateral velocity of the air jet near the roof was much higher than the longitudinal velocity. Therefore, the methane occurring along the roof was blown away and could not accumulate at the top of the bolter miner, creating a high-risk area (in which methane concentration $> 0.75\%$) near the walking part of the bolter miner area. Then, as the airflow started to stabilize in the whole tunnel, the methane flow became increasingly affected by buoyancy: the methane occurring along the tunnel floor rose gradually, eventually reaching the tunnel roof. At $T = 149$ s, methane with concentration $> 0.35\%$ began to diffuse throughout the tunnel: the corresponding temporal–spatial evolution fitting equation can be expressed as $L_{\text{Methane}} = -0.0028T^4 + 0.1215T^3 - 1.8628T^2 + 17.346T - 14.449$. According to the mathematical relationship between the methane diffusion distance and time, before $T = 40$ s, methane with concentration $> 0.35\%$ diffused quickly in the tunnel. Over time, methane gradually entered a stable airflow field: the mixing of methane with the airflow field led to a gradual reduction of the methane diffusion speed. Finally, at $T = 296$ s, the methane concentration in the tunnel stabilized at $\sim 0.59\%$.

Influence of different air duct outlet positions on air pollution

To effectively solve the problem of air pollution in tunnels, the distribution law of the airflow–dust–methane multi-phase coupling between the pressure air outlet and the working face at different distances (L_p) was simulated and the optimal L_p for eliminating pollution was determined.

Influence of the air duct outlet position on the airflow field characteristics

The overall distribution of airflow at different air duct outlet positions during the tunnel excavation process is shown in Fig. 7: with the increase of L_p , the range of the three vortices first decreased, then increased, and finally decreased. The L_p ranges of each vortices range change were $L_p < 12$ m, $12 \text{ m} < L_p < 16$ m, and $L_p > 16$ m.

Figure 8 shows that the jet velocity of pressure air inflow had a basically stable range around that outlet itself; afterward, however, the air velocity decayed. Notably, with the attenuation for a certain distance, the air velocity fluctuated within a certain range after passing through the vortex area that continuously sucked in the reentry airflow; then,

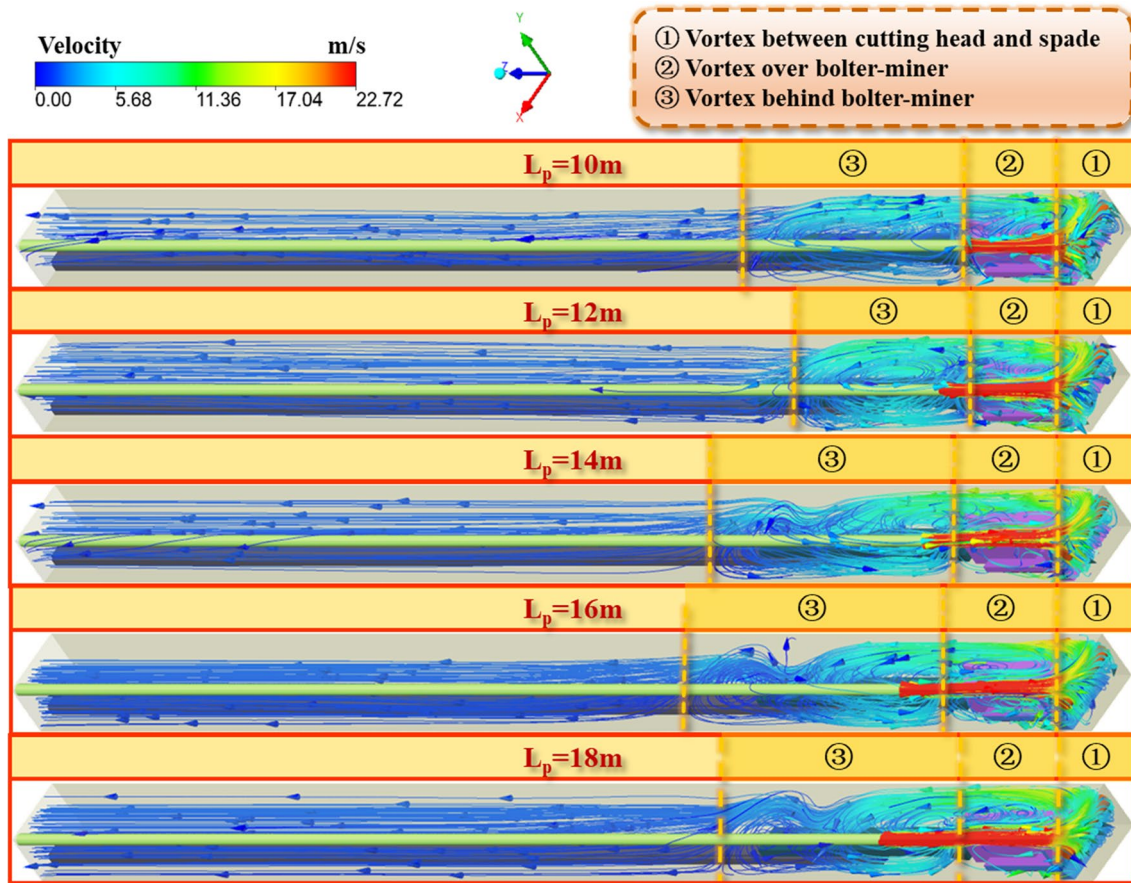


Fig. 7 Overall distribution of airflow in tunnel under different L_p

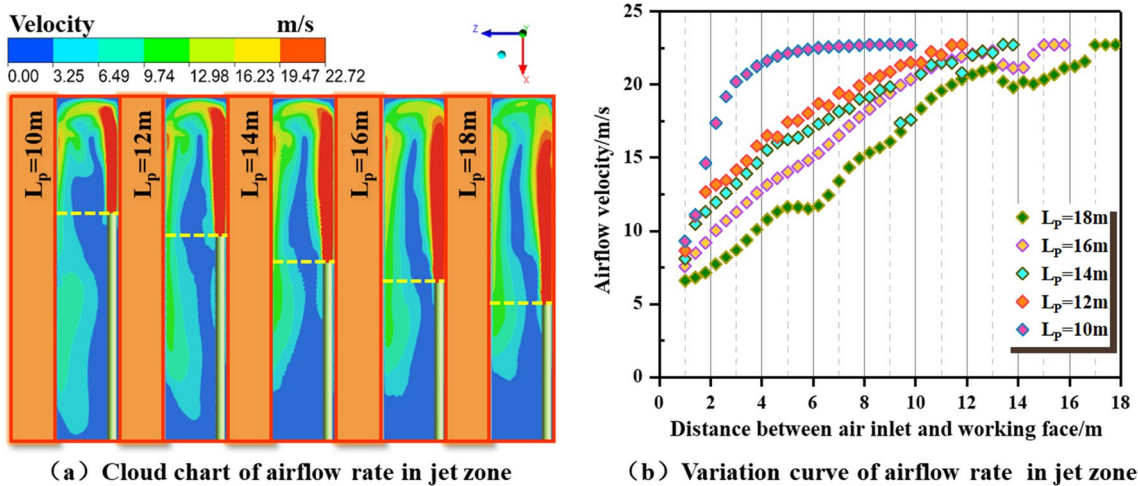
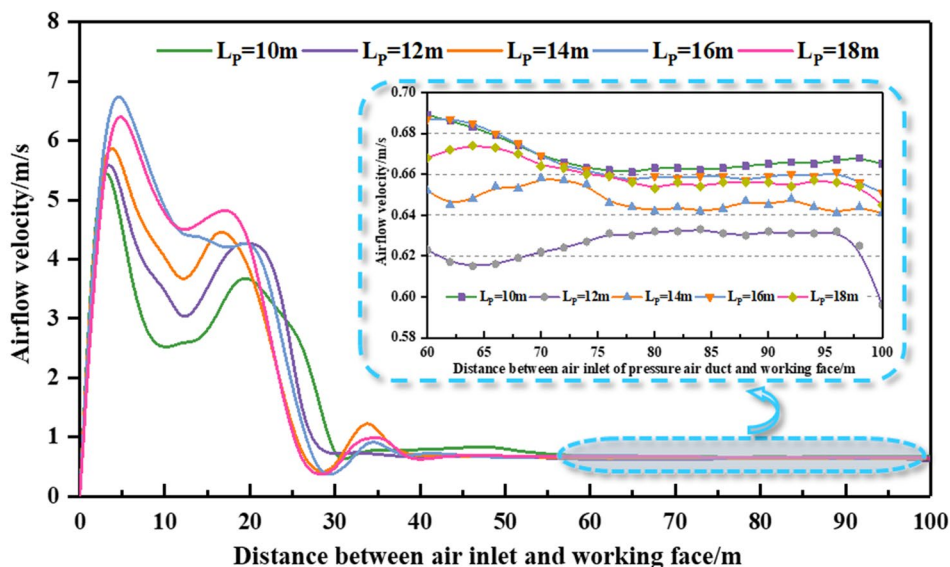


Fig. 8 Comparison diagram of airflow rate in jet zone

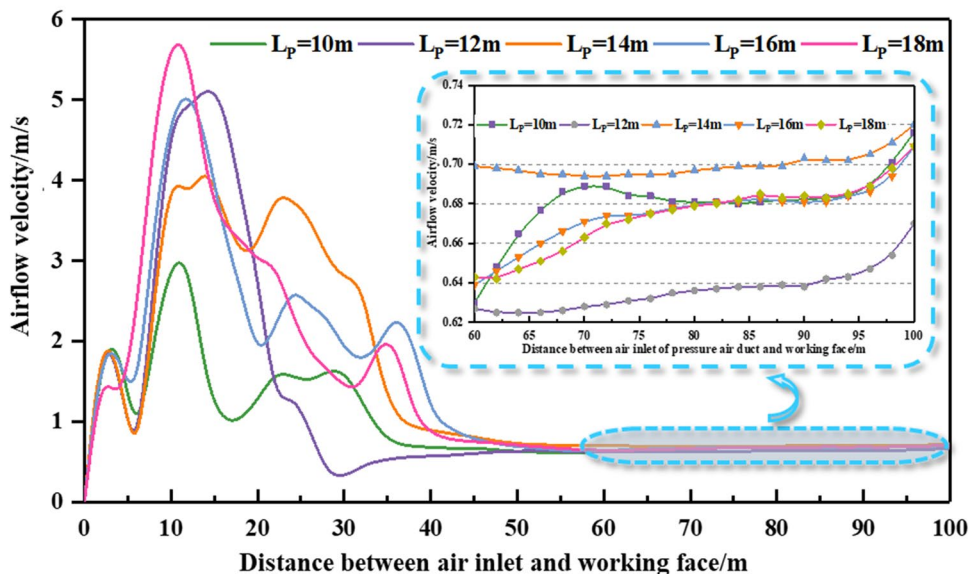
the attenuation of the air velocity became relatively slow. When $14\text{ m} \leq L_p \leq 16\text{ m}$, the attenuation velocity of the airflow was relatively slow, indicating that the vortex had a greater impact within this range.

The above dust–methane diffusion analysis demonstrated that the dust–methane concentration on the air duct side was significantly higher than that on the opposite side. Therefore, we mainly focused on the air velocity variation

Fig. 9 Diagram of airflow rate variation



(a) Airflow rate at axial height of air duct (Opposite side of air duct)



(b) Airflow rate at breathing zone (Opposite side of air duct)

curve of the breathing zone on the left side of the tunnel and on the axial height of the air duct on this side by considering different L_p values (Fig. 9). Figure 8 shows, after the airflow turned back from the working face and was affected by the three vortices and the equipment energy, there was a period of velocity fluctuation near the bolter-miner; after this, the velocity stabilized at ~ 0.65 m/s. In the velocity fluctuation stage, the peak value of air velocity was the highest when $14\text{ m} \leq L_p \leq 16\text{ m}$; in this case, the air velocity during the fluctuation process was higher than under other conditions (a condition which is useful for the control of dust–methane air pollution).

Influence of the air duct outlet position on dust distribution

When considering different L_p , the time required by dust for reaching the tunnel exit for the first time was ~ 110 s, while that required for its stabilization in the tunnel was ~ 220 s. The dust distributions under these two conditions are shown in Fig. 10. The diffusion of dust in the tunnel was closely related to the airflow velocity and its local characteristics. As already mentioned in the previous Sect. 4.1, the range of the three vortices was larger when $12\text{ m} < L_p < 16\text{ m}$. Meanwhile, the airflow attenuation

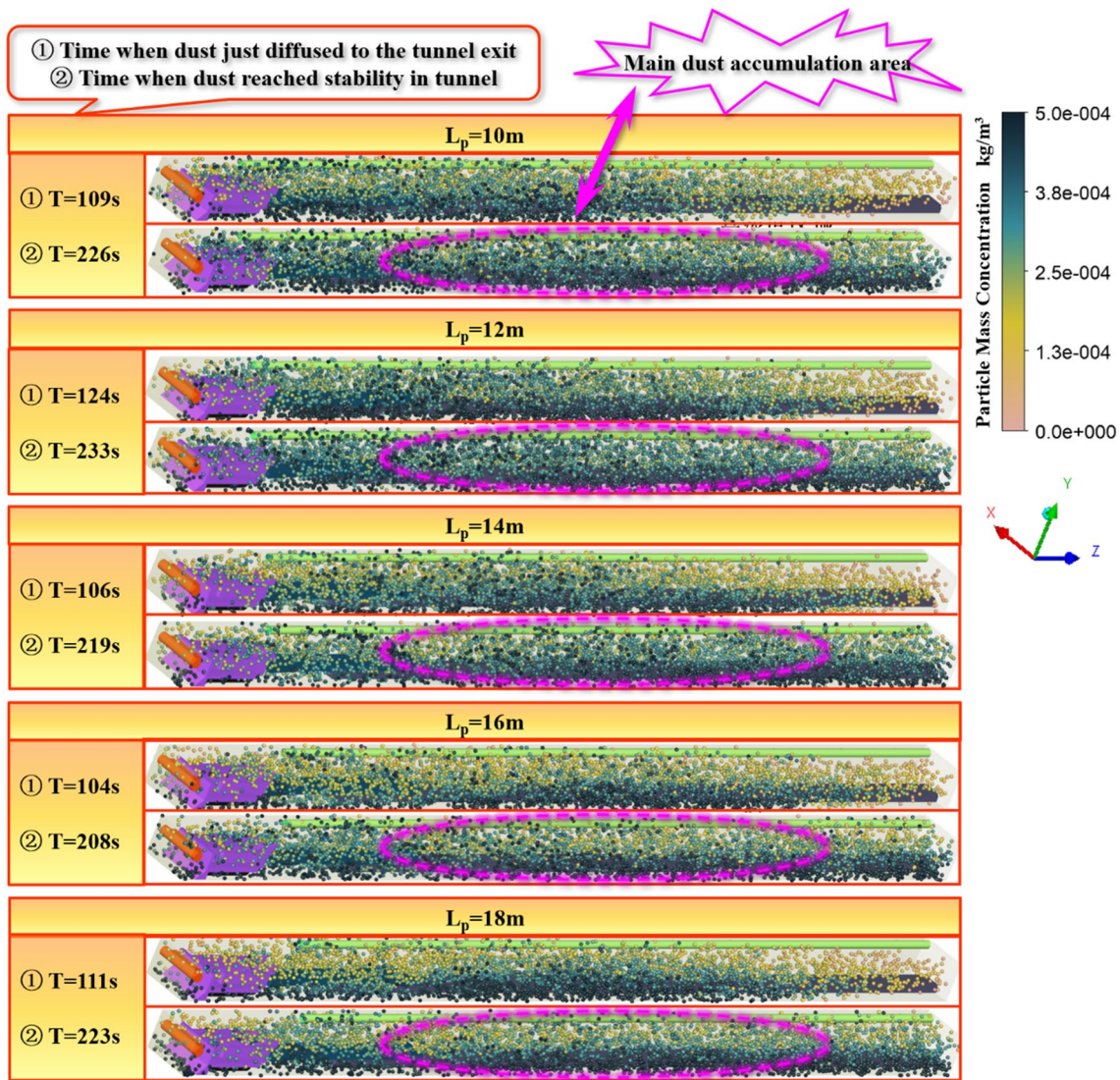


Fig. 10 Diagram of dust diffusion in tunnel under different L_p

velocity was relatively low when $14 \text{ m} \leq L_p \leq 16 \text{ m}$: under these conditions, air velocity and, hence, the ability of air to carry dust, reached their maximum. Therefore, as shown in Fig. 10, dust concentration was significantly higher in the middle of the tunnel than in other areas; moreover, dust concentration decreased with the increase of L_p , but rose again when L_p exceeded 16 m.

The above dust diffusion study demonstrated the frequent occurrence of serious dust accumulation at the bottom of tunnels and the harmfulness of dust in the breathing zone for workers. With the ultimate aim of improving the working environment, we mainly focused on the dust distributions in the breathing zone ($Y = 1.55 \text{ m}$) and at the bottom of the tunnel. As shown in Figs. 11 and 12,

dust accumulated at the working face, behind the bolter-miner, and on the left wall of the tunnel. The cloud diagram (Fig. 11) clearly shows how the variations of dust concentration for different L_p could be divided into three stages, which were consistent with the variation ranges of the three airflow vortices previously mentioned. When $L_p < 12 \text{ m}$, the dust concentration in the three accumulation areas increased with the increase of L_p ; when $12 \text{ m} < L_p < 16 \text{ m}$, it decreased with the increase of L_p ; when $L_p > 16 \text{ m}$, it increased with the increase of L_p . Therefore, the best dust removal effect was obtained when $14 \text{ m} \leq L_p < 16 \text{ m}$.

Figure 12 quantitatively compares the dust concentrations at the bottom and in breathing zone at the side of the tunnel with and without air duct for different L_p . Due to

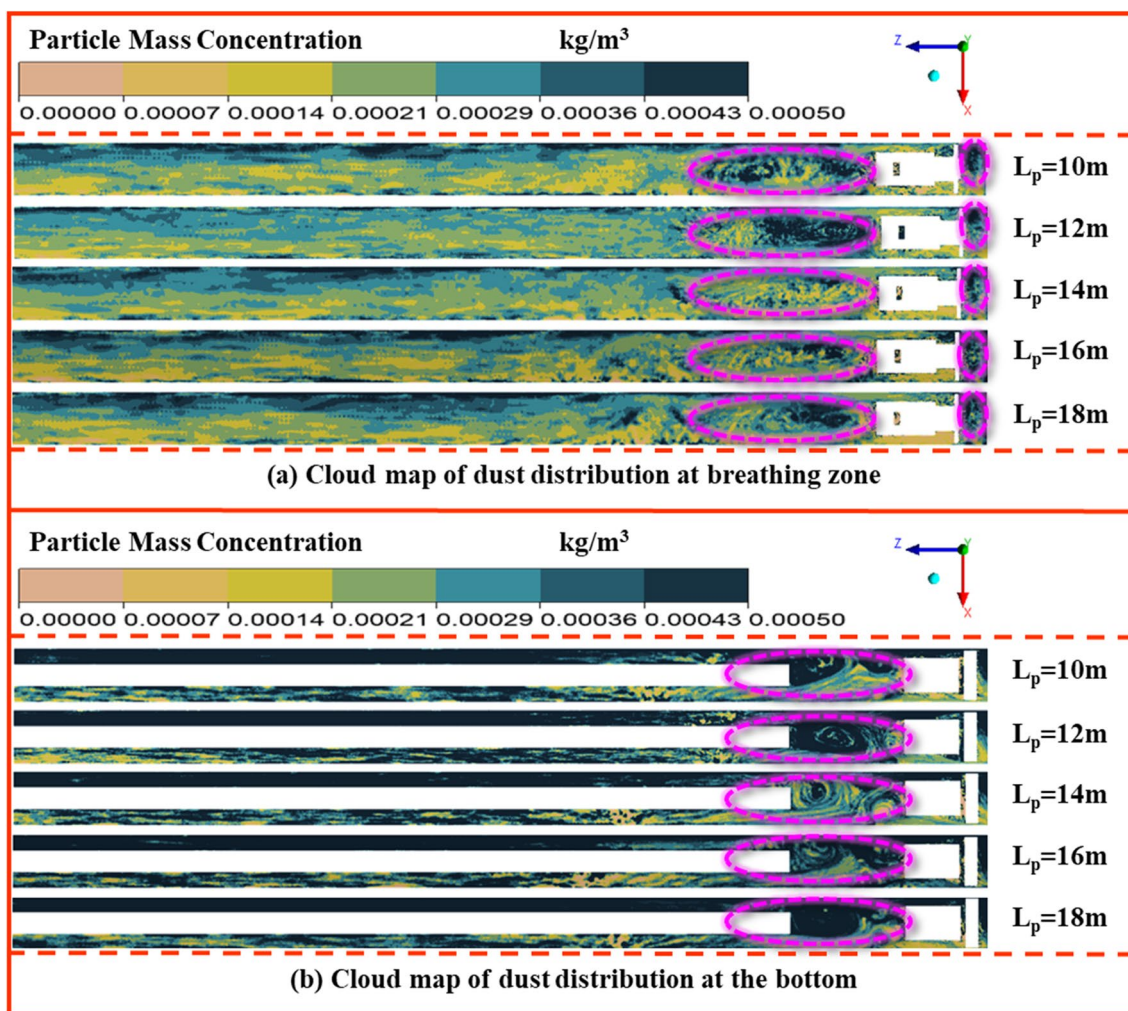


Fig. 11 Diagram of dust pollution at the bottom and breathing zone under different L_p

the limited air velocity at the corner between the working face and the left wall of the tunnel, the dust concentration reached there its peak value. When $14\text{ m} \leq L_p < 16\text{ m}$, the dust concentration at the breathing zone was controlled at $432.6\text{--}481.3\text{ mg/m}^3$, while that at the bottom was $551.5\text{--}623.5\text{ mg/m}^3$. Under other L_p conditions, the dust concentration reached values $> 500\text{ mg/m}^3$ in the breathing zone, $> 700\text{ mg/m}^3$ at the bottom of the tunnel, even more than 900 mg/m^3 at the bottom of the tunnel. After this peak, the dust concentration decreased significantly: the curve fluctuations indicated that, in the case of $14\text{ m} \leq L_p < 16\text{ m}$, the dust concentrations were lower than

in the other cases considered. In conclusion, the optimal dust removal effect was obtained for $14\text{ m} \leq L_p \leq 16\text{ m}$.

Influence of the air duct outlet position on methane distribution

The buoyancy of methane resulted into its accumulation along the tunnel roof; moreover, methane concentration changed greatly in the jet area due to the influence of the air duct inflow. Therefore, we focused on the methane distribution along the roof, in the jet area, and in the breathing zone ($Y=1.55\text{ m}$) for different L_p (Figs. 13 and 14). Methane concentration was influenced by its own buoyancy and mixing with the airflow after

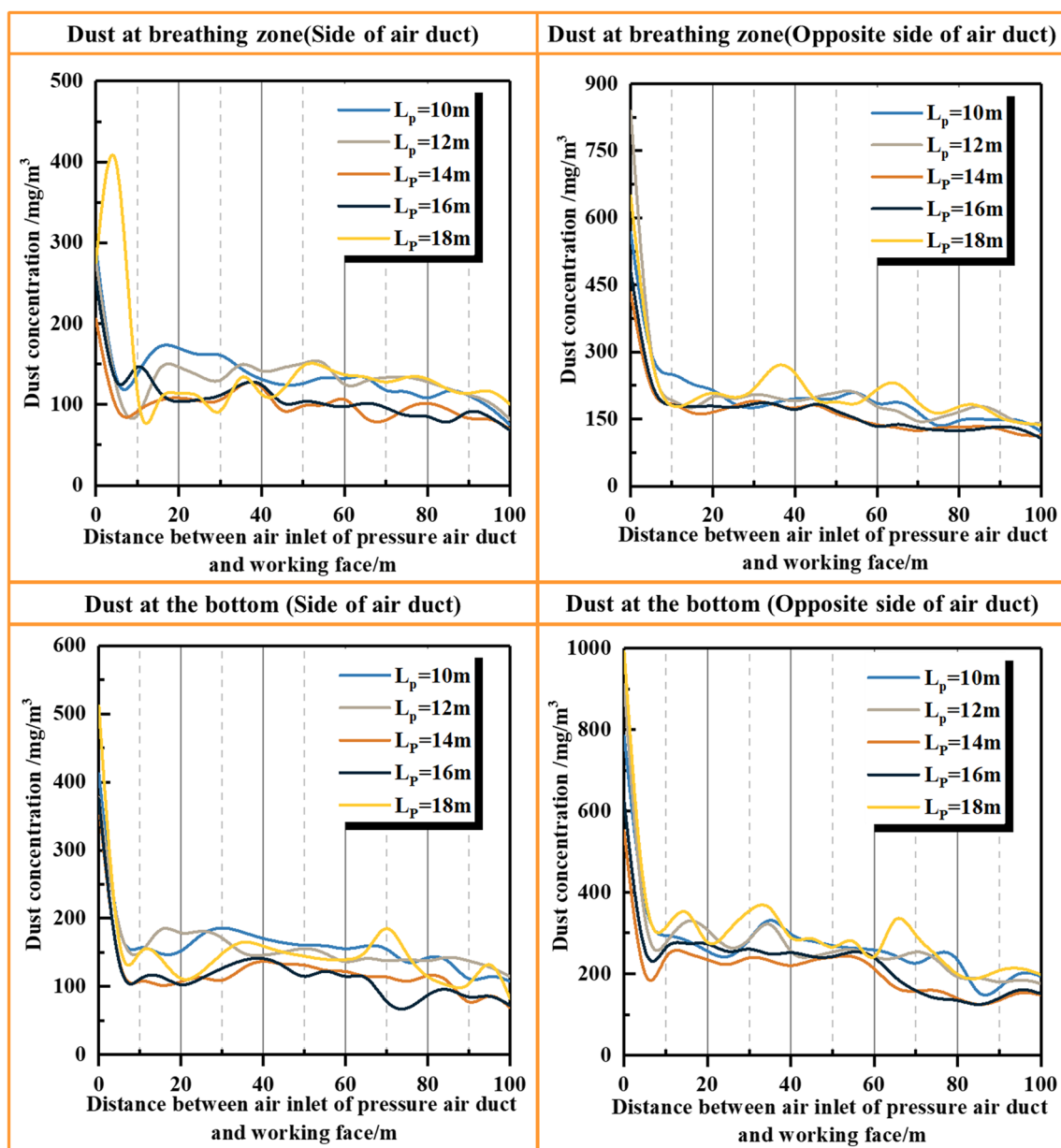


Fig. 12 Variation map of dust concentration at the bottom and breathing zone under different L_p

convection, and its stable concentration was closely related to the airflow velocity at the top of the tunnel and the initial airflow velocity at the pressure outlet. We noticed that the larger the L_p value, the larger were the jet area and the range of high airflow velocity, which had a significant impact on the initial diffusion of methane along the roof. Overall, as shown in the figure below, the stability of methane concentration in the tunnel decreased with the increase of L_p . When $L_p > 14$ m, methane concentration was $< 0.6\%$; meanwhile, when $L_p = 18$ m,

methane concentration was $\sim 0.49\%$. The distribution range of high-risk methane concentrations near the bolter miner was influenced by the local airflow field and changes in airflow velocity. With the increase of L_p , the high-risk area near the bolter miner (with methane concentration $> 0.75\%$) gradually shrank; however, when $L_p = 18$ m, the range of the high-risk area increased. In conclusion, the optimal methane dilution effect was observed for $14 \text{ m} \leq L_p \leq 16 \text{ m}$.

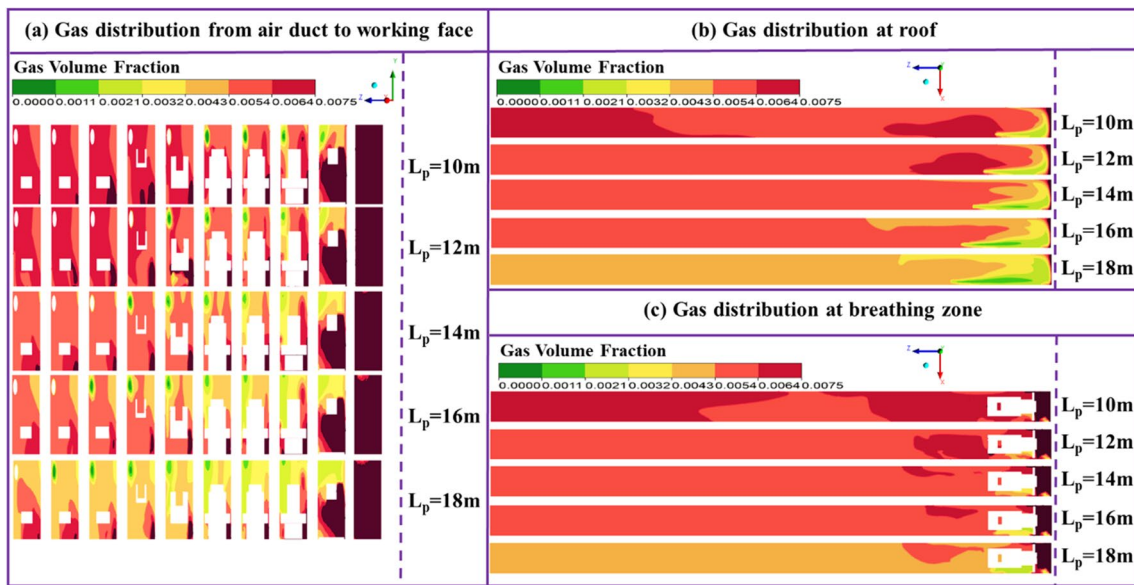


Fig. 13 Cloud map of gas distribution under different L_p

Fig. 14 Variation map of gas concentration at breathing zone, roof under different L_p

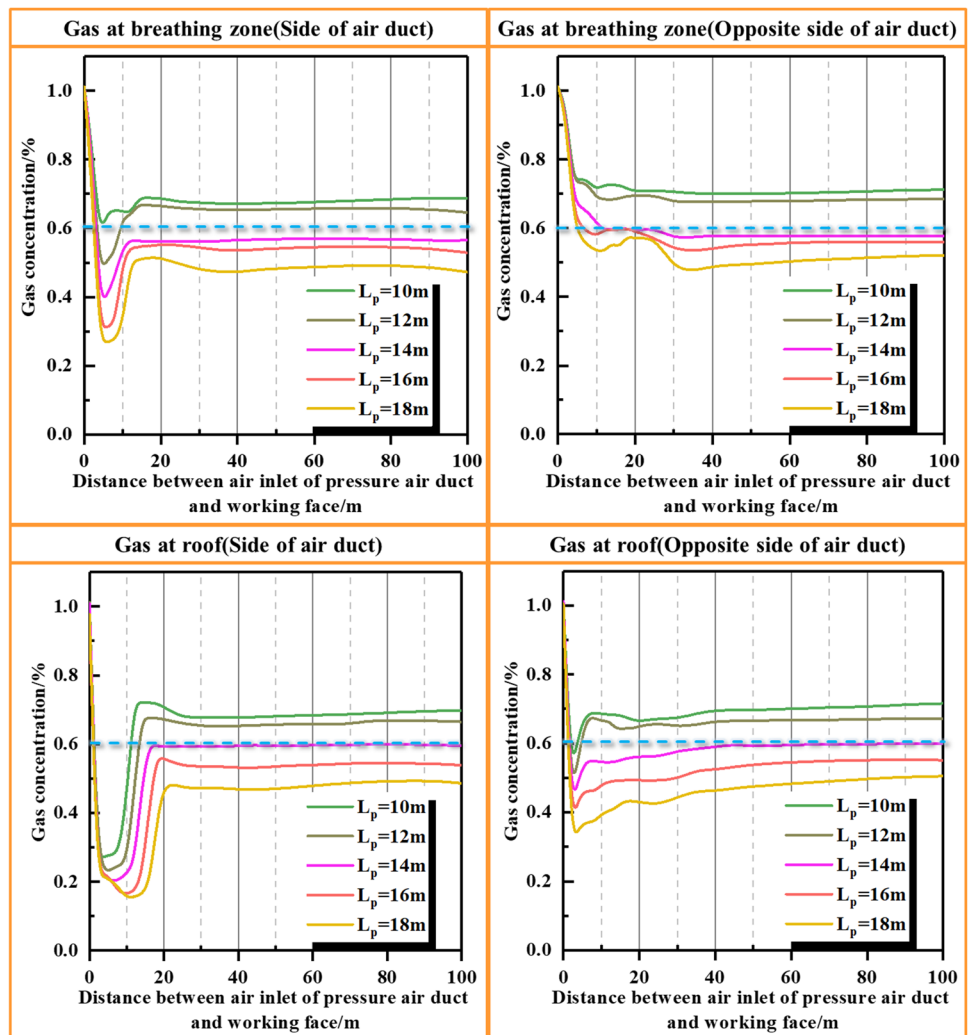
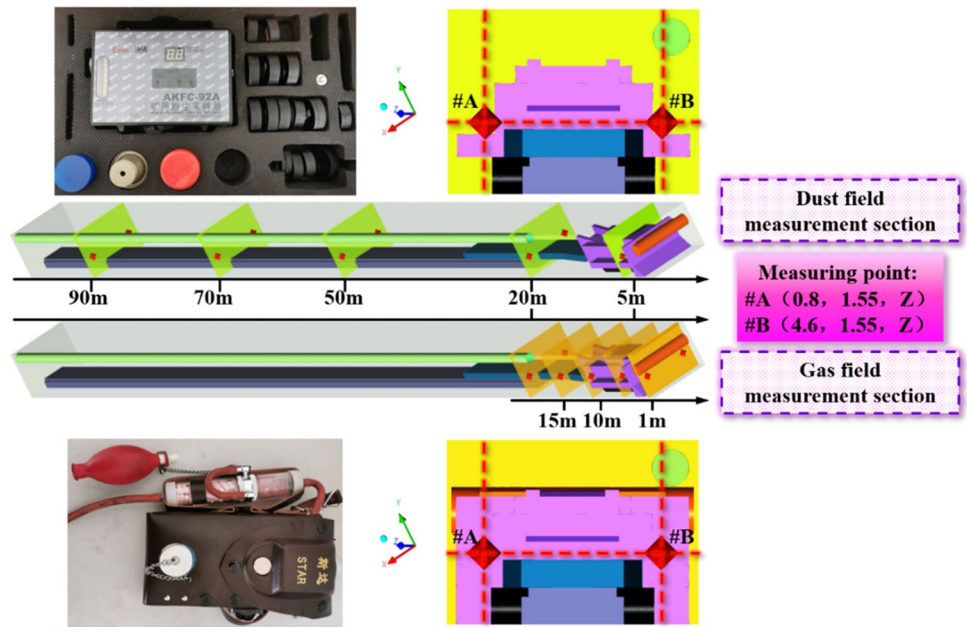


Fig. 15 Diagram of field measurement section of dust-gas and related equipment



Field measurement results and analysis

To verify the authenticity of the above simulation results, we first measured the real dust and methane concentrations in the mine of Baode Coal Mining Co., Ltd for different

L_p , and then compared the measured and simulated values.

After verifying the consistency of the equipment layout of the excavation face with the simulation model, we set several measuring points within the breathing zone. The coordinates of the measuring points were expressed

Table 2 Gas concentration at each measuring point of cross-section

Coordinates of measuring points	Gas concentration	Distances between the pressure air outlet and the working face/m				
		10	12	14	16	18
(0.8, 1.55, 1)	Simulation results/%	0.96	0.96	0.96	0.95	0.94
	Measured results/%	0.90	0.91	0.88	0.87	0.85
(0.8, 1.55, 5)	Simulation results/%	0.74	0.73	0.68	0.63	0.61
	Measured results/%	0.83	0.79	0.74	0.69	0.65
(0.8, 1.55, 10)	Simulation results/%	0.71	0.69	0.61	0.58	0.54
	Measured results/%	0.75	0.67	0.54	0.53	0.48
(0.8, 1.55, 15)	Simulation results/%	0.73	0.68	0.60	0.59	0.55
	Measured results/%	0.70	0.66	0.63	0.56	0.53
(0.8, 1.55, 20)	Simulation results/%	0.67	0.64	0.64	0.64	0.57
	Measured results/%	0.72	0.65	0.61	0.55	0.52
(4.6, 1.55, 1)	Simulation results/%	0.83	0.80	0.79	0.78	0.72
	Measured results/%	0.85	0.78	0.74	0.69	0.68
(4.6, 1.55, 5)	Simulation results/%	0.60	0.53	0.42	0.32	0.27
	Measured results/%	0.65	0.58	0.40	0.35	0.30
(4.6, 1.55, 10)	Simulation results/%	0.66	0.63	0.55	0.50	0.34
	Measured results/%	0.69	0.67	0.50	0.47	0.37
(4.6, 1.55, 15)	Simulation results/%	0.67	0.66	0.56	0.54	0.49
	Measured results/%	0.65	0.60	0.52	0.51	0.47
(4.6, 1.55, 20)	Simulation results/%	0.68	0.67	0.56	0.54	0.48
	Measured results/%	0.64	0.61	0.51	0.49	0.46

Table 3 Dust concentration at each measuring point of cross-section

Coordinates of measuring points	Dust concentration	Distances between the pressure air outlet and the working face/m				
		10	12	14	16	18
(0.8, 1.55, 5)	Simulation results/mg/m ³	236.1	214.1	185.9	184.9	190.7
	Measured results/mg/m ³	257.5	233.2	163.4	171.6	201.3
(0.8, 1.55, 20)	Simulation results/mg/m ³	196.1	201.3	168.4	160.5	196.2
	Measured results/mg/m ³	184.3	213.5	151.8	156.3	173.6
(0.8, 1.55, 50)	Simulation results/mg/m ³	191.0	209.2	158.6	160.4	197.0
	Measured results/mg/m ³	183.4	221.6	166.3	153.8	211.9
(0.8, 1.55, 70)	Simulation results/mg/m ³	157.8	176.3	138.8	157.3	189.8
	Measured results/mg/m ³	176.6	193.8	123.5	142.5	176.2
(0.8, 1.55, 90)	Simulation results/mg/m ³	167.4	165.3	133.4	135.2	165.6
	Measured results/mg/m ³	178.6	174.4	119.5	128.4	177.3
(4.6, 1.55, 5)	Simulation results/mg/m ³	120.9	128.4	94.9	96.8	130.7
	Measured results/mg/m ³	133.6	116.5	87.4	85.3	118.5
(4.6, 1.55, 20)	Simulation results/mg/m ³	155.6	145.9	99.3	100.4	123.5
	Measured results/mg/m ³	163.2	156.7	105.3	109.1	136.0
(4.6, 1.55, 50)	Simulation results/mg/m ³	124.6	149.9	103.0	107.7	156.3
	Measured results/mg/m ³	138.5	135.4	112.9	101.5	167.8
(4.6, 1.55, 70)	Simulation results/mg/m ³	126.0	133.5	110.8	105.8	140.7
	Measured results/mg/m ³	133.2	126.4	107.5	112.1	157.2
(4.6, 1.55, 90)	Simulation results/mg/m ³	114.2	134.7	77.6	101.3	132.8
	Measured results/mg/m ³	105.7	128.4	83.8	95.6	145.7

in the format (X, Y, Z): X represented the distance of the point from the right wall of the tunnel, Y that from the tunnel floor (always 1.55 m), and Z that from the working face (Fig. 15). Since the methane concentration changed greatly near the bolter miner and then stabilized, the methane measuring points were concentrated in the proximity of the bolter miner ($Z = 1, 5, 10, 15$, and 20 m). For the monitoring of dust, it was very important to measure the concentration distribution along the whole tunnel: we selected $Z = 5, 20, 50, 70$, and 90 m. To effectively compare the difference between the air duct side and the non-air duct side, we set two measuring points in each measuring section: #A (0.8, 1.55, Z) and #B (4.6, 1.55, Z). To reduce errors during the on-site sampling measurements, three methane and dust measurements were performed at each measuring point. The average of these three values was then calculated and used for further analysis.

An AKFC-92A mine dust sampler, based on the dust concentration weighing method, was used to sample and measure dust particles. Before sampling, we loaded a weighed clean filter membrane into the pre-catcher of the sampler. During sampling, a fixed volume of dusty air was extracted: dust was retained on the filter membrane and gradually accumulated. At the end of the sampling process, we calculated the total mass of dust as the difference

between the original and the final weight of the filter membrane. A CJG10 optical interference gas detector was used to measure methane concentration in the mine. Before performing any measurement, the instrument was inspected for air tightness, zero alignment, and other parameters. After that, a suction balloon capable of inhaling methane-containing air was activated 5–10 times at the measuring point. Then, we read the methane concentration (expressed in integer and decimal values) through the eyepiece and the micro-reading disk after turning the micro-adjusting screw.

Tables 2, 3 show the measured and simulated values for each measuring point. Figures 16, 17 compare the measured and simulated values and the concentration distribution at each measuring point, while Fig. 18 shows the errors between the measured and simulated values at each measuring point. These errors were mostly < 10%. Notably, the errors of dust concentration varied between 2.62 and 12.10%, those of methane concentration between 2.41 and 14.06%, and the average error between them was < 10%. This suggests that the simulated dust and methane concentrations were similar to those measured on site and, hence, that our simulation data are reliable. The data in Tables 2, 3 and Figs. 16, 17 demonstrate how the dust and methane concentration distribution characteristics and the pollutant distribution characteristics under different L_p

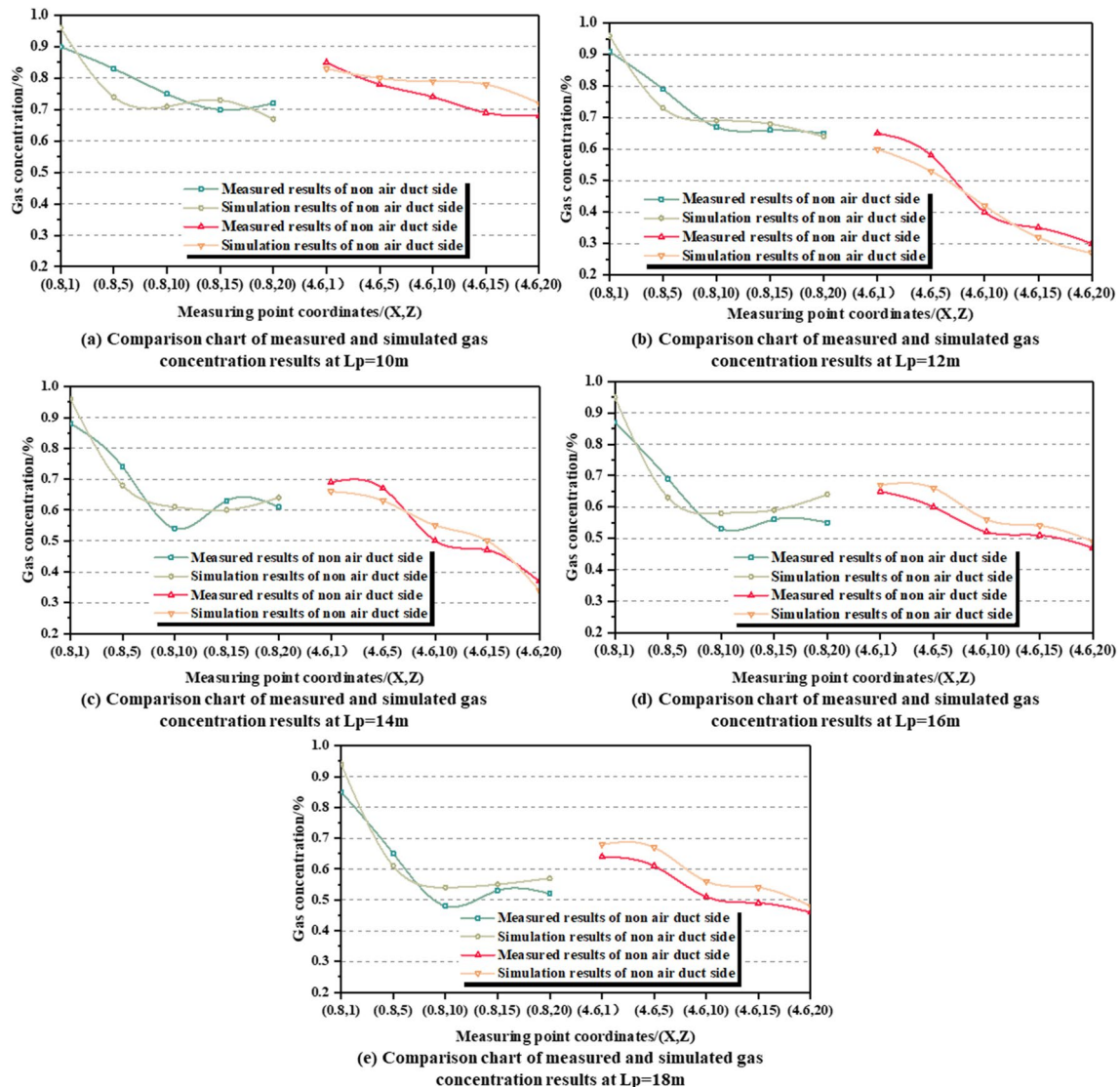


Fig. 16 Comparison chart of measured and simulated methane concentration results

conditions (obtained through simulation analysis) agree with the field measurement results. To sum up, dust concentration was particularly high along the side of the tunnel without air duct, methane concentration was particularly high near the bolter miner, the stabilized methane concentration decreased with the increase of L_p , and the lowest dust concentration in the accumulation area occurred where $14\text{ m} \leq L_p < 16\text{ m}$. Overall, the simulated distribution of pollutants is similar to that obtained from the field measurements, indicating that the optimization parameters of the ventilation system obtained in this study are reliable. In conclusion, our simulation results are solid and provide a good theoretical basis for describing the actual situation.

Conclusion

- (1) Using the CFD software, we studied the diffusion law and the pollution distribution of dust and methane in an airflow–dust–methane coupling field under the action of a single-forced ventilation system in an excavation and anchor synchronous tunnel. Our analyses showed the occurrence of three vortex fields in the airflow field near the bolter miner (at the cutting head, above the bolter miner, and behind the bolter miner, respectively). After passing through the transition flow field, a stable airflow field was formed (airflow velocity = 0.65 m/s). Dust accumulation areas were mainly located at the working face,

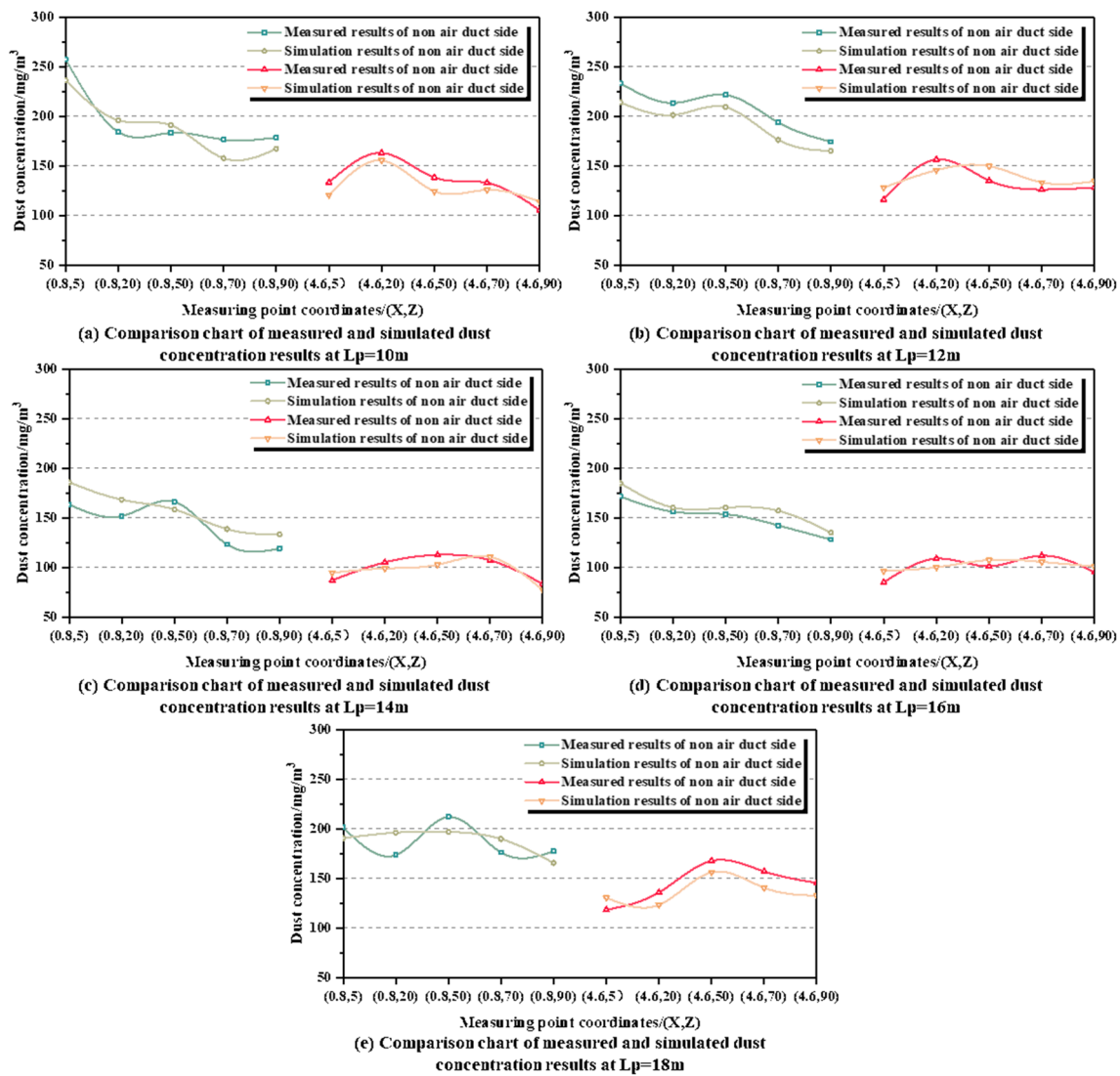


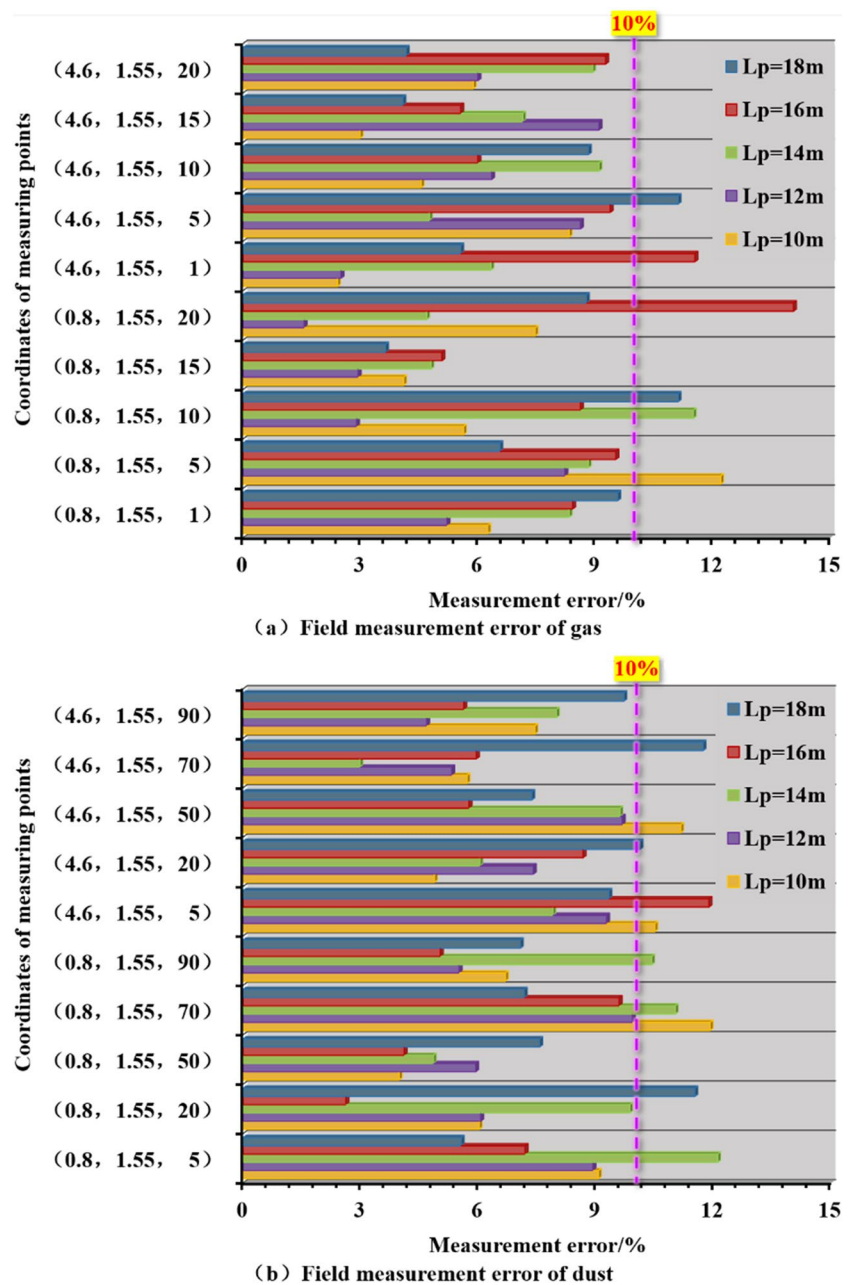
Fig. 17 Comparison chart of measured and simulated dust concentration results

behind the bolter miner, and above the floor (on the left side of the tunnel). High-risk areas (with methane concentration $> 0.75\%$) were mainly located near the walking part of the bolter miner. The temporal-spatial evolution law and the fitting mathematical relationship between dust and methane under the dust-methane coupling effect were revealed, and the mathematical relationship between time and space was clarified.

- (2) In order to improve the tunnel working environment, the control effects of dust and methane pollution for different L_p values were compared and analyzed, determining the optimal air duct blowdown distance. We

found that when $14\text{ m} \leq L_p \leq 16\text{ m}$, the peak dust concentration was the smallest; after this peak, the dust concentration was significantly lower than under other conditions (i.e., the airflow had a good dust removal effect). At the same time, the methane concentration was $< 0.6\%$ and the high-risk area near the walking part of the bolter miner (with methane concentration $> 0.75\%$) was the smallest (i.e., the airflow had a good methane dilution effect). In summary, the best simultaneous control of dust and methane (i.e., the best improvement of the tunnel operating environment) was achieved when the pressure air outlet distance (L_p) was between 14–16 m.

Fig. 18 Distribution map of relative error in field measurement of dust-gas



Despite the interesting results of this study, we focused on the control of dust and methane pollution in a methane-containing tunnel based on a single-forced ventilation system. To achieve an even better simultaneous control of dust and methane, future studies should aim at improving the effectiveness of ventilation control systems. Therefore, the next step is to improve the ventilation system of the excavation tunnel (where high methane emissions occur), while effectively controlling the coupling pollution of dust and methane.

Authors contribution All authors contributed to the study conception and design. Material preparation, data collection, and analysis were performed by Qianqian Xue, Wen Nie, Yun Hua, and Faxin Li. Assist in numerical simulation, field investigation, and validation were performed by Lidian Guo, Qiang Liu, Ning Sun, Chenwang Jiang, and Fengning Yu. The first draft of the manuscript was written by Qianqian Xue, and all authors commented on previous versions of the manuscript. All authors read and approved the final manuscript.

Funding This work has been funded by the National Natural Science Foundation of China (no. 52174191 and 51874191), the National Key R&D Program of China (2017YFC0805201), Qingchuang Science and Technology Project of Shandong Province University (2020KJD002), and Taishan Scholars Project Special Funding (TS20190935).

Data availability All data generated or analyzed during this study are included in this published article.

Declarations

Ethics approval and consent to participate Not applicable.

Consent for publication Not applicable.

Competing interests The authors declare no competing interests.

References

- Abbasi T, Abbasi SA (2007) Dust explosions—cases, causes, consequences, and control. *J Hazard Mater* 140:7–44. <https://doi.org/10.1016/j.jhazmat.2006.11.007>
- Adel T, Farhang S, Faramarz DA, Ali M (2016) Numerical modeling of gas flow in coal pores for methane drainage. *J Sustain Min* 15:95–99. <https://doi.org/10.1016/j.jsm.2016.10.001>
- Candra KJ, Pulung SA, Sadashiv MA (2014) Dust dispersion and management in underground mining faces. *Int J Min Sci Technol* 24:39–44
- Cui CQ, Wang B, Zhao YX, Wang Q, Sun ZM (2019) China's regional sustainability assessment on mineral resources: results from an improved analytic hierarchy process-based normal cloud model. *J Clean Prod* 210:105–120. <https://doi.org/10.1016/j.jclepro.2018.10.324>
- Chang P, Xu G, Huang JX (2020) Numerical study on DPM dispersion and distribution in an underground development face based on dynamic mesh. *Int J Min Sci Technol* 30:471–475. <https://doi.org/10.1016/j.ijmst.2020.05.005>
- Chang P, Xu G, Zhou FB, Mullins D, Abishekd S, Chalmers D (2019) Minimizing DPM pollution in an underground mine by optimizing auxiliary ventilation systems using CFD. *Tunn Undergr Sp Tech* 87:112–121. <https://doi.org/10.1016/j.tust.2019.02.014>
- Du JS (2017) Study on the concentration distribution of gas in heading face and optimization of duct arrangement. Chongqing University of Science and Technology, ChongQing
- Diego I, Torno S, Toraño J, Menéndez M, Gent M (2011) A practical use of CFD for ventilation of underground works. *Tunn Undergr Space Technol* 26:189–200. <https://doi.org/10.1016/j.tust.2010.08.002>
- Fan G, Gui CG, Teng HX, Tang JH, Niu HW, Zhou FB, Liu C, Hu SD, Li SH (2020) Dispersion characteristics of dust pollutant in a typical coal roadway under an auxiliary ventilation system. *J Clean Prod* 275:122889. <https://doi.org/10.1016/j.jclepro.2020.122889>
- Fan L, Liu SM (2021) Respirable nano-particulate generations and their pathogenesis in mining workplaces: a review. *Int J Coal Sci Technol* 8:179–198
- Finkelman RB, Wolfe A, Hendryx MS (2021) The future environmental and health impacts of coal. *Energy* 2:99–112. <https://doi.org/10.1016/j.engeos.2020.11.001>
- Gui CG, Geng F, Tang JH, Niu HW, Zhou FB, Liu C (2020) Gas–solid two-phase flow in an underground mine with an optimized air-curtain system: a numerical study. *P Rcess Saf Environ* 140:137–150
- Hasheminasab F, Bagherpour R, Aminossadati SM (2019) Numerical simulation of methane distribution in development zones of underground coal mines equipped with auxiliary ventilation. *Tunn Undergr Space Technol* 89:68–77
- Huang QM, Li J, Liu SM, Wang G (2021) Experimental study on the adverse effect of gel fracturing fluid on gas sorption behavior for Illinois coal. *Int J Coal Sci Technol* 8:1250–1261
- Huang W, Yan ZT, Sun F, Zhao BB, Xue SF, Zhou B (2022) Particle flow simulation of Brazilian splitting failure characteristics of layered shale. *Shandong Univ Sci Technol* 41(06):74–82. <https://doi.org/10.16452/j.cnki.sdkjzk.2022.06.008>
- Hua Y, Nie W, Liu Q, Liu XF, Liu CY, Zhou WW, Yu FN (2022) Analysis of diffusion behavior of harmful emissions from trackless rubber-wheel diesel vehicles in underground coal mines. *Int J Min Sci Technol* 32(6):1285–1299. <https://doi.org/10.1016/j.ijmst.2022.09.004>
- Hu SY, Liao Q, Wang HT, Feng GR, Xu LH, Huang YS, Shao H, Gao Y, Hu F (2019) Gas–solid two-phase flow at high-gassy fully mechanized within high gassy coal seam. *J China Coal Soc* 44:3921–3930
- Han FW, Zhang JY, Zhao Y, Han JH (2019) Experimental investigation on the interaction process between coal particles and foam. *AIP Adv* 9:015023. <https://doi.org/10.1063/1.5080469>
- Jia LX (2017) Application of dry dust catcher on working panel of digging anchor. *Coal Mine Mach* 38:123–126 1003–0794(2017)03–0123–04
- Ji SS, Ye HJ (2018) Study on methane control technology of roadway with tunneling and anchor reinforcement. *China Energy Environ Prot* 40:69–72+77 1003–0506(2018)08–0069–04
- Kurnia JC, Xu P, Sasmito AP (2016) A novel concept of enhanced gas recovery strategy from ventilation air methane in underground coal mines e A computational investigation. *J Nat Gas Sci Eeg* 35:661–672
- Kurnia JC, Sasmito AP, Mujumdar AS (2014) CFD simulation of methane dispersion and innovative methane management in underground mining faces. *Appl Math Model* 38:3467–3484
- Lu Y, Akhtar S, Sasmito AP, Kurnia JC (2017) Prediction of air flow, methane, and coal dust dispersion in a room and pillar mining face. *Int J Min Sci Technol* 27:657–662
- Liu JL, Chen JG (2019) Nozzle selection and dust reduction effect analysis of continuous miner in 11219 heading face of Xiaojihan coal mine. *Mod Min* 597:147–150+175
- Liu Q, Nie W, Hua Y, Peng HT, Liu CQ, Wei CH (2019) Research on tunnel ventilation systems: dust Diffusion and Pollution Behaviour by air curtains based on CFD technology and field measurement. *Build Environ* 147:444–460. <https://doi.org/10.1016/j.buildenv.2018.08.061>
- Li XC, Hu YF, Zhang W (2013) Study of dust suppression by atomized water from high-pressure sprays in Mines. *J Central South Univ* 44:862–866
- Liu T, Liu S (2020) The impacts of coal dust on miners' health: A review. *Environ Res* 190:109849
- Li YC, Li Z, Gao L (2014) Arrangement of air duct in tunneling working face based on the distribution laws of airflow and dust. *J China Coal Soc* 39:130–135
- Li XC, Luo HQ, Hu HB, Wang BC, Wei T, Lv XF (2015) Pressure fluctuation characteristics and gas–liquauid coupling of self-swash dust collector. *J China Coal Soc* 12:3001–3006 <https://doi.org/10.13225/j.cnki.jccs.2015.0264>
- Liu A, Liu SM, Liu P, Wang K (2021a) Water sorption on coal: effects of oxygen-containing function groups and pore structure. *Int J Coal Sci Technol* 8:983–1002
- Liu CY, Nie W, Luo CY, Hua Y, Yu FN, Niu WJ, Zhang X, Zhang SB, Xue QQ, Sun N, Jiang CW (2023) Numerical study on temporal and spatial distribution of particulate matter under multi-vehicle working conditions. *Sci Total Environ* 862:160710. <https://doi.org/10.1016/j.scitotenv.2022.160710>
- Liu JG, Wang S, Jin LZ, Wang TY, Zhou ZH, Xu JG (2021b) Water-retaining properties of NCZ composite dust suppressant and its wetting ability to hydrophobic coal dust. *Int J Coal Sci Technol* 8:240–247
- Liu Q, Wang Q, Wu P, Wang JX, Lv XJ (2022) Research progress in application of red mud in cementitious materials. *Shandong*

- Univ Sci Technol 41(03):66–74. <https://doi.org/10.16452/j.cnki.sdkjzk.2022.03.008>
- Lafuente A, Recio J, Hueso RO, Gallardo A, Pérez-Corona ME, Manrique E, Durán J (2020) Simulated nitrogen deposition influences soil greenhouse gas fluxes in a Mediterranean dryland. *Sci Total Environ* 737:139610 <https://doi.org/10.1016/j.scitotenv.2020.139610>
- Lauder BE, Spalding DB (1974) The numerical computation of turbulent flows. *Comput Methods Appl Mech* 3:269–289. [https://doi.org/10.1016/0045-7825\(74\)90029-2](https://doi.org/10.1016/0045-7825(74)90029-2)
- Li YZ, Su HT, Ji HJ, Cheng WY (2020) Numerical simulation to determine the gas explosion risk in longwall goaf areas: a case study of Xutuan Colliery. *Int J Min Sci Technol* 30:875–882. <https://doi.org/10.1016/j.ijmst.2020.07.007>
- Lu XX, Shen C, Xing Y, Zhang H, Wang CY, Shi GY, Wang MY (2022) The spatial diffusion rule and pollution region of disorganized dust in the excavation roadway at different roadheader cutting positions. *Powder Technol* 396:167–180
- Ma D, Duan HY, Zhang JX, Bai HB (2022) A state-of-the-art review on rock seepage mechanism of water inrush disaster in coal mines. *Int J Coal Sci Technol* 9:50
- Mishra DP, Panigrahi DC, Kumar P (2018) Computational investigation on effects of geo-mining parameters on layering and dispersion of methane in underground coal mines — a case study of Moonidih Colliery. *J Nat Gas Sci Eeg* 58:110–124
- Niu HM, Yang T (2019) Optimization and application of dust control system with long pressure and short pumping in continuous mining face. *Mod Min* 598:199–200+204
- Nie W (2022) Comparative study of dust pollution and air quality of tunnelling anchor integrated machine working face with different ventilation. *Tunnelling and Underground Space Technology* 122:104377. <https://doi.org/10.1016/j.tust.2022.104377>
- Niu WJ, Nie W, Yuan MY, Bao Q, Zhou WW, Yan JY, Yu FN, Liu CY, Sun N, Xue QQ (2021) Study of the microscopic mechanism of lauryl glucoside wetting coal dust: environmental pollution prevention and control. *J Hazard Mater* 412:125223. <https://doi.org/10.1016/j.jhazmat.2021.125223>
- Nie W, Yang B, Du T, Peng HT, Zhang X, Zhang YL (2022) Dynamic dispersion and high-rise release of coal dust in the working surface of a large-scale mine and application of a new wet dust reduction technology. *J Clean Prod* 351:131356. <https://doi.org/10.1016/j.jclepro.2022.131356>
- Nie W, Zhang YL, Guo LD, Zhang X, Peng HT, Chen DW (2023a) Research on airborne air curtain dust control technology and air volume optimization. *Process Saf Environ Prot* 172:113–123. <https://doi.org/10.1016/j.psep.2023.01.073>
- Nie W, Yi SX, Xu CW, Zhang SB, Peng HT, Ma QX, Guo C, Cha XP, Jiang CW (2023b) Numerical simulation analysis of a combined wind-fog dust removal device in return air roadways based on an orthogonal test. *Powder Technol* 413:117890. <https://doi.org/10.1016/j.powtec.2022.117890>
- Nie W, Cha XP, Bao Q, Peng HT, Xu CW, Zhang SB, Zhang X, Ma QX, Guo C, Yi SX, Jiang CW (2023c) Study on dust pollution suppression of mine wind-assisted spray device based on orthogonal test and CFD simulation. *Energy* 263:125590. <https://doi.org/10.1016/j.energy.2022.125590>
- Niu WJ, Nie W, Bao Q, Tian QF, Li RX, Zhang XH, Yan X, Lian J (2023d) Development and characterization of a high efficiency bio-based rhamnolipid compound dust suppressant for coal dust pollution control. *Environ Pollut* 330:121792. <https://doi.org/10.1016/j.envpol.2023.121792>
- Nie W, Jiang CW, Sun N, Guo LD, Xue QQ, Liu Q, Liu CY, Cha XP, Yi SX (2023e) Analysis of multi-factor ventilation parameters for reducing energy air pollution in coal mines. *Energy* 278:127732. <https://doi.org/10.1016/j.energy.2023.127732>
- Niu WJ, Nie W, Bao Q, Tian QF, Li RX, Zhang XH, Yan X, Lian J (2023) Study on the effects of surfactants on the interface characteristics and wettability of lignite. *Powder Technol* 423:118482. <https://doi.org/10.1016/j.powtec.2023.118482>
- Nie W, Tian QF, Niu WJ, Li RX, Bao Q, Zhang XH, Yan X, Lian J (2023) Synergistic effect of binary mixture of anionic nonionic surfactant on inhibiting coal dust pollution: experiment and simulation. *J Environ Chem Eng* 11(3):110099. <https://doi.org/10.1016/j.jece.2023.110099>
- Nie W, Yan X, Yu FN, Bao Q, Li N, Zhou WW, Niu WJ, Tian QF (2023) Study on the effect of Ce–Cu doping on Mn/γ-Al O catalyst for selective catalytic reduction in NO with NH₃. *Environ Geochem Health*. <https://doi.org/10.1007/s10653-023-01582-z>
- Omid R, Farnoush M, Seid SG, John T, Davoud DM, Coulon F, Omid AN, Bui DT (2020) Identifying sources of dust aerosol using a new framework based on remote sensing and modelling. *Sci Total Environ* 737:139508 <https://doi.org/10.1016/j.scitotenv.2020.139508>
- Paluchamy B, Mishra DP, Panigrahi DC (2021) Airborne respirable dust in fully mechanised underground metalliferous mines e Generation, health impacts and control measures for cleaner production. *J Clean Prod* 296:126524 <https://doi.org/10.1016/j.jclepro.2021.126524>
- Peng HT, Nie W, Zhang X, Xu CW, Meng X, Cheng WM, Liu Q, Hua Y (2022) Research on the blowing-spraying synergistic dust removal technology for clean environment in large-scale mechanization coal mine. *Fuel* 324:124508. <https://doi.org/10.1016/j.fuel.2022.124508>
- Ren B, Yuan L, Zhou G, Li SL, Meng QZ, Wang K, Jiang BY, Yu GF (2022) Effectiveness of coal mine dust control: A new technique for preparation and efficacy of self-adaptive microcapsule suppressant. *Int J Min Sci Technol* 32(6):1181–1196. <https://doi.org/10.1016/j.ijmst.2022.09.006>
- Seaman CE, Shahan MR, Beck TW, Mischler SE (2020) Design of a water curtain to reduce accumulations of float coal dust in longwall returns. *Int J Min Sci Technol* 30:443–447. <https://doi.org/10.1016/j.ijmst.2020.05.001>
- Shu LY, Yuan L, Li XQ, Xue WT, Zhu NN, Liu ZS (2023) Response characteristics of gas pressure under simultaneous static and dynamic load: Implication for coal and gas outburst mechanism International. *Int J Min Sci Technol* 33(2):155–171. <https://doi.org/10.1016/j.ijmst.2022.11.005>
- Tu QY, Cheng YP, Xue S, Ren T, Cheng X (2021) Energy-limiting factor for coal and gas outburst occurrence in intact coal seam. *Int J Min Sci Technol* 9 <https://doi.org/10.1016/j.ijmst.2021.05.009>
- Torno S, Torano J, Álvarez-Fernández I (2020) Simultaneous evaluation of wind flow and dust emissions from conveyor belts using computational fluid dynamics (CFD) modelling and experimental measurements. *Powder Technol* 373:310–322
- Trechera P, Morena T, Córdoba P, Morena N, Zhuang XG, Li BQ, Li J, Shanguan YF, Kandler K, Dominguez AO, Kellye F, Querol X (2020) Mineralogy, geochemistry and toxicity of size-segregated respirable deposited dust in underground coal mines. *J Hazard Mater* 399:122935 <https://doi.org/10.1016/j.jhazmat.2020.122935>
- Wang CX (2010) Effects of the air-flow direction on the distribution and accumulation of the gas in the inclined coalmine tunnel. Henan Polytechnic University, HeNan
- Wang DZ, Zhu DQ, Pan J, Guo ZQ, Yang CC, Tian HY, Xue YX (2022) Integration of preparation of K Na-embedded activated carbon and reduction of Zn-bearing dusts. *Int J Min Sci Technol* 32(3):627–636. <https://doi.org/10.1016/j.ijmst.2022.03.003>
- Wei WL (2018) Temporal and spatial evolution of respirable dust distribution in fully mechanized top coal caving face. Shandong University of Science and Technology, ShanDong

- Wang B, Huang ZK, Hu SY, Wang L, Yang PJ, Lu CL (2022) Rheological law and 3D constitutive model of coal rock containing gas. *Shandong Univ Sci Technol* 41(05):60–67. <https://doi.org/10.16452/j.cnki.sdkjzk.2022.05.007>
- Wang ZW, Li SG, Ren T, Wu JM, Lin HF, Shuang HQ (2019a) Respirable dust pollution characteristics within an underground heading face driven with continuous miner—a CFD modelling approach. *J Clean Prod* 217:267–283. <https://doi.org/10.1016/j.jclepro.2019.01.273>
- Wang PF, Tian C, Liu RH, Wang J (2019b) Mathematical model for multivariate nonlinear prediction of SMD of X-type swirl pressure nozzles. *Process Saf Environ* 125:228–237. <https://doi.org/10.1016/j.psep.2019.03.023>
- Xu CW, Nie W, Liu ZQ, Peng HT, Yang SB, Liu Q (2019) Multi-factor numerical simulation study on spray dust suppression device in coal mining process. *Energy* 182:544–558. <https://doi.org/10.1016/j.energy.2019.05.201>
- Xu CW, Nie W, Peng HT, Zhang SB, Liu F, Yi SX, Cha XP, Mwabaima FI (2023) Numerical simulation of the dynamic wetting of coal dust by spray droplets. *Energy* 270:126667. <https://doi.org/10.1016/j.energy.2023.126667>
- Xue LM, Zhang WJ, Zheng ZX, Liu Z, Meng S, Li HQ, Du YL (2021) Measurement and influential factors of the efficiency of coal resources of China's provinces: based on Bootstrap-DEA and Tobit. *Energy* 221:119763 <https://doi.org/10.1016/j.energy.2021.119763>
- Xu G, Luxbacher KD, Ragab S, Xu JL, Ding XH (2016) Computational fluid dynamics applied to mining engineering: a review. *Int J Min Reclam Environ* 31:251–275. <https://doi.org/10.1080/17480930.2016.1138570>
- Xu Y, Li ZJ, Liu HS, Zhai XW, Li RR, Song PF, Jia MT (2020) A model for assessing the compound risk represented by spontaneous coal combustion and methane emission in a gob. *J Clean Prod* 273:122925 <https://doi.org/10.1016/j.jclepro.2020.122925>
- Xu QF, Peng SJ, Xu J, Jiao F, Cheng L, Jia L, Yang HL, Yang Y, Liu RL, Ramakrishna S (2023) Study on time effect of acidified pulverized coal micro components and discussion on mathematical correlation of influencing factors. *Fuel* 342:127842. <https://doi.org/10.1016/j.fuel.2023.127842>
- Zhang R, Liu SM, Zheng SY (2021) Characterization of nano-to-micron sized respirable coal dust: particle surface alteration and the health impact. *J Hazard Mater* 413:125447 <https://doi.org/10.1016/j.jhazmat.2021.125447>
- Zheng YL, Zhang QB, Zhao J (2016) Challenges and opportunities of using tunnel boring machines in mining. *Tunn Undergr Space Technol* 57:287–299. <https://doi.org/10.1016/j.tust.2016.01.023>
- Zhou LH, Pritchard C, Zheng Y (2015) CFD modeling of methane distribution at a continuous miner face with various curtain setback distances. *Int J Min Sci Technol* 25:635–640. <https://doi.org/10.1016/j.ijmst.2015.05.018>

Publisher's note Springer Nature remains neutral with regard to jurisdictional claims in published maps and institutional affiliations.

Springer Nature or its licensor (e.g. a society or other partner) holds exclusive rights to this article under a publishing agreement with the author(s) or other rightsholder(s); author self-archiving of the accepted manuscript version of this article is solely governed by the terms of such publishing agreement and applicable law.